Geophysical Journal International

Geophys. J. Int. (2021) **224,** 1724–1741
Advance Access publication 2020 November 20
GJI Seismology

doi: 10.1093/gji/ggaa561

Azimuthal anisotropy in Bayesian surface wave tomography: application to northern Cascadia and Haida Gwaii, British Columbia

Jeremy M. Gosselin [1], Pascal Audet,[1] Andrew J. Schaeffer,[2] Fiona A. Darbyshire [3] and Clément Estève[1]

[1] *Department of Earth and Environmental Sciences, University of Ottawa, ON, Canada. E-mail: jeremy.gosselin@uottawa.ca*
[2] *Geological Survey of Canada, Pacific Division, Sidney, BC, Canada*
[3] *Centre de recherche GEOTOP, Université du Québec à Montréal, QC, Canada*

Accepted 2020 November 18. Received 2020 September 14; in original form 2020 May 6

SUMMARY

Surface wave tomography is a valuable tool for constraining azimuthal anisotropy at regional scales. However, sparse and uneven coverage of dispersion measurements make meaningful uncertainty estimation challenging, especially when applying subjective model regularization. This paper considers azimuthal anisotropy constrained by measurements of surface wave dispersion data within a Bayesian trans-dimensional (trans-d) tomographic inversion. A recently proposed alternative model parametrization for trans-d inversion is implemented in order to produce more realistic models than previous studies considering trans-d surface wave tomography. The reversible-jump Markov chain Monte Carlo sampling technique is used to numerically estimate the posterior probability density of the model parameters. Isotropic and azimuthally anisotropic components of surface wave group velocity maps (and their associated uncertainties) are estimated while avoiding model regularization and allowing model complexity to be determined by the data information content. Furthermore, data errors are treated as unknown, and solved for within the inversion. The inversion method is applied to measurements of surface wave dispersion from regional earthquakes recorded over northern Cascadia and Haida Gwaii, a region of complex active tectonics but highly heterogeneous station coverage. Results for isotropic group velocity are consistent with previous studies that considered the southern part of the study region over Cascadia. Azimuthal anisotropic fast-axis directions are generally margin-parallel between Vancouver Island and Haida Gwaii, with a small change in direction and magnitude along the margin which may be attributed to the changing tectonic regime (from subduction to transform tectonics). Estimated errors on the dispersion data (solved for within the inversion) reveal a correlation between surface wave period and the dependence of data errors on travel path length. This paper demonstrates the value of considering azimuthal anisotropy within Bayesian tomographic inversions. Furthermore, this work provides structural context for future studies of tectonic structure and dynamics of northern Cascadia and Haida Gwaii, with the aim of improving our understanding of seismic and tsunami hazards.

Key words: Inverse theory; Seismic anisotropy; Surface waves and free oscillations.

1 INTRODUCTION

Seismic anisotropy is the dependence of seismic wave speeds on the direction of propagation, and manifests the coherent alignment of rock fabrics via deformation in the crust and upper mantle. As such, measuring seismic anisotropy is valuable for understanding Earth's evolution, dynamics and structure. Deformation can result in lattice preferred orientation (sometimes called crystallographic orientation) of intrinsically anisotropic minerals, and shape preferred orientation of discontinuous and heterogeneous Earth structure (Montagner & Guillot 2002). Seismically observable anisotropy in the crust is generally attributed to rock microfractures, the alignment of anisotropic minerals with major foliations and layered sequences of sedimentary rocks (Babuska & Cara 1991). Anisotropy in the upper

mantle may be explained by the alignment of anisotropic olivine minerals (Montagner & Anderson 1989; Babuska & Cara 1991). When subjected to a simple shear force, olivine aggregates develop a lattice preferred orientation via dislocation creep, with a fast-axis direction parallel to the direction of shear (Karato *et al.* 2008). For these reasons, seismic anisotropy reflects the record of deformation within the Earth and provides useful constraint on the dynamics of the crust and mantle.

Seismic anisotropy can be estimated from single station techniques to much larger spatial scales. Observations of shear wave splitting from refracted teleseismic body wave (e.g. SKS) phases offer a relatively simple method for constraining 1-D anisotropy beneath a seismograph station (e.g. Vinnik *et al.* 1989, 1992; Savage 1999). Shear wave splitting is also commonly considered using local earthquake data in order to constrain crustal anisotropy (e.g. Balfour *et al.* 2012). However, since these measurements represent the depth-integrated effect of anisotropy beneath the station, they are typically interpreted as the result of a single layer of anisotropy, with a trade-off between the thickness of this layer and the anisotropic intensity. The effects of multiple anisotropic layers beneath a station are challenging to interpret. Single-station azimuthal dependence has also been observed in teleseismic receiver function studies and has been attributed to anisotropic layering structure (e.g. Savage 1998; Audet 2015). For such methods, the lateral resolution of anisotropy depends on the spatial distribution of seismograph stations that record body waves.

Azimuthal anisotropy has been constrained using surface waves via tomographic inversions at regional (e.g. Darbyshire & Lebedev 2009; Darbyshire *et al.* 2018; McLellan *et al.* 2018) and global (e.g. Schaeffer *et al.* 2016) scales. Such tomographic studies constrain both the lateral and depth variations in anisotropy, since different periods of surface waves are sensitive to structure at different depth ranges in the Earth. To date, these studies utilize linearized and regularized inversions, where the resulting model depends on the choice and level of regularization. Such methods must simultaneously solve for the distribution of isotropic seismic velocities, in addition to seismic anisotropy, with the caveat that anisotropic structures are not as well resolved as isotropic features. As a result, anisotropy within these models must be regularized more strongly. Such choices make quantification of uncertainty of the various isotropic and anisotropic features, and their interpretation, difficult. Furthermore, regularization of anisotropy within a model is challenging. As discussed in Schaeffer *et al.* (2016), this is particularly important in polar regions where standard smoothing and gradient damping methods may produce model artifacts (where anisotropic structures appear to circle the poles or point towards them), due to the significant changes in ray azimuth direction (relative to north) along travel paths at these latitudes.

Understanding and quantifying the uncertainties in estimated anisotropy allows for more reliable interpretation of these structures. In recent years, Bayesian methods have become popular for solving seismic tomography problems in studies considering surface wave (e.g. Bodin & Sambridge 2009; Bodin *et al.* 2012; Zulfakriza *et al.* 2014; Galetti *et al.* 2017) and body wave (e.g. Piana Agostinetti *et al.* 2015) traveltime data. Bayesian inversion allows for rigorous uncertainty quantification in geophysical inverse problems. Bayesian inversion is a probabilistic approach in which model parameters (e.g. the distribution of isotropic seismic velocities and anisotropy) along with the observed data are treated as random variables. These model parameters are constrained by data as well as prior information, which may be informative (thereby providing additional constraint) or uninformative (allowing the solution to be entirely constrained by data information content). The posterior probability density (PPD) of the model parameters is the solution to the inverse problem. Typically, the PPD is numerically estimated using Markov chain Monte Carlo (McMC) methods (Mosegaard & Tarantola 1995; Brooks *et al.* 2011). A preferred model and associated uncertainty can be determined from features of the PPD.

Studies that have considered Bayesian seismic tomography have typically applied an adaptive model parametrization that allows the spatial complexity of the model to be determined by the data information content. In such a framework, the number of model parameters is treated as an unknown within the inversion. These methods are commonly referred to as trans-dimensional (trans-d), as the PPD spans multiple possible model dimensions (i.e. a different number of model parameters). In this case, the generalized reversible-jump Markov chain Monte Carlo (rjMcMC) algorithm is used to numerically estimate the PPD (Green 1995, 2003). Trans-dimensional inversion allows for increased model complexity where it is required by the data, and estimates of model uncertainty include the uncertainty in the model complexity/parametrization. Consequently, this method avoids subjective regularization choices that can preclude meaningful uncertainty analysis, as well as avoiding user-based choices of a particular model complexity.

This work aims to incorporate azimuthal anisotropy in a trans-d Bayesian tomographic inversion of surface wave dispersion data in order to avoid subjective regularization procedures, as well as to quantify the uncertainty in the orientation of seismically detectable rock fabrics. Our work is motivated by the modelling challenges posed by data collected along the west coast of Canada. The complex interactions between the North American (NA), Pacific (PA) and Juan de Fuca (JdF) plates along the coast of British Columbia produces significant seismicity, as well as a poorly understood transition between the Cascadia subduction zone and the transpressive Haida Gwaii region (Fig. 1). Resolving seismic velocity structure (isotropic and anisotropic) in this region using standard single-station passive seismological techniques is complicated by the sparsity of station coverage to the west of the plate boundaries, with a large gap between Vancouver Island and Haida Gwaii. Body wave derived velocity models (i.e. tomography, receiver functions) suffer from insufficient lateral sampling of the 3-D volume. However, surface waves can efficiently sample volumes where station coverage is sparse. We demonstrate our novel inversion approach through synthetic experiments, and apply this method to resolve anisotropic surface wave velocities across northern Cascadia and Haida Gwaii. We consider surface wave dispersion measurements obtained from recordings of regional earthquakes over several decades. These measurements allow for robust estimation of anisotropic Rayleigh-wave group velocity maps at periods between 15 and 50 s. Our results demonstrate the value of this novel inversion technique and provide an initial step towards resolving a full, 3-D, seismic velocity model in future work, with the incorporation of additional data sets. Furthermore, this work provides broad structural context for future seismic station deployments (both onshore and offshore) to study the tectonic structure and dynamics of the region, with the aim of improving our understanding of seismic and tsunami hazards.

2 TECTONIC SETTING

The west coast of British Columbia is the most seismically active region in Canada, with a history of large earthquakes and tsunamis and the potential for hosting future large events. The region comprises a number of active tectonic boundaries including the northernmost

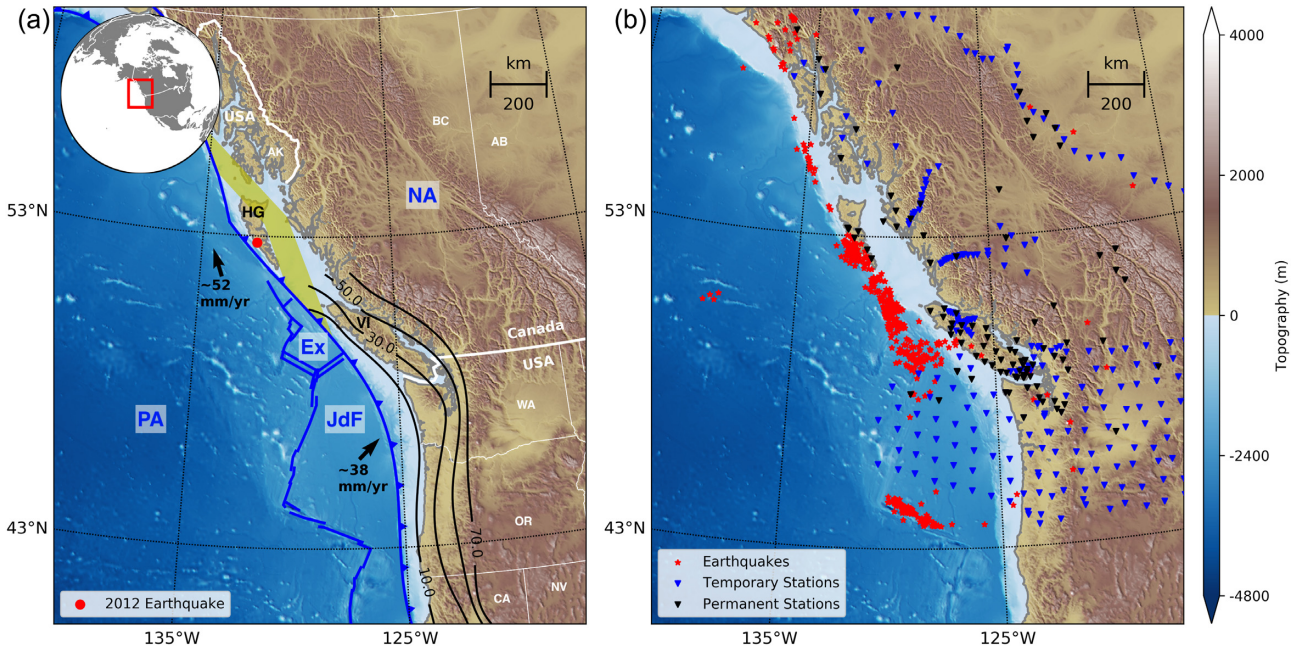

Figure 1. Tectonic setting of coastal British Columbia (a). Contours define the top of the JdF plate beneath NA (in kilometres) from Bostock *et al.* (2019). Tectonic boundaries are shown in blue. The yellow shaded region marks the possible extent of subduction of the PA plate beneath Haida Gwaii from plate kinematics (Smith *et al.* 2003). Plate motions are shown by black arrows and are relative to NA (Kreemer *et al.* 2003). HG and VI represent Haida Gwaii and Vancouver Island, respectively. Political boundaries are shown in white. AK, BC, AB, WA, OR, CA and NV represent Alaska, British Columbia, Alberta, Washington, Oregon, California and Nevada, respectively. The red circle marks the epicentre of the 2012 Haida Gwaii Earthquake. Broad-band seismic stations considered in this work, and seismicity with magnitude greater than 4.5 between 2000 and 2019 are shown in (b).

extent of the Cascadia subduction zone, which has historically produced large megathrust earthquakes and associated tsunamis (Nelson *et al.* 1995; Satake *et al.* 1996, 2003). North of Cascadia, the termination of subduction involves a number of triple junctions that are poorly understood (Fig. 1). This produces significant seismicity and a complex system of transform faulting (Hutchinson *et al.* 2019), as well as the breakup and possible capture of the Explorer (Ex) microplate (formerly part of the JdF plate) by the NA Plate (Braunmiller & Nábělek 2002; Audet *et al.* 2008; Savard *et al.* 2020). Near Haida Gwaii, along the northernmost coast of British Columbia, the transpressive interaction between the PA and the NA plates produces significant seismicity, including Canada's two largest instrumentally recorded earthquakes (Bostwick 1984; Cassidy *et al.* 2014). Margin-parallel motion between the PA and NA plates is predominantly accommodated by the strike-slip Queen Charlotte Fault (QCF). North of Haida Gwaii, the QCF continues into Alaska as the Fairweather fault. The orientation of the QCF with respect to the direction of plate motion requires that a component of convergence of approximately 15 mm yr^{-1} exists across the margin (Kreemer *et al.* 2003). However, the nature of how plate convergence is accommodated across Haida Gwaii is unsettled.

A significant body of geophysical evidence including seismic velocity structure, thermal and gravity modelling suggests convergence is accommodated by subduction, or underthrusting, of PA beneath NA (Hyndman 2015; Gosselin *et al.* 2015, and references therein). On 28 October 2012, a moment-magnitude 7.8 thrust earthquake occurred off the west coast of Haida Gwaii producing a large local tsunami (Leonard & Bednarski 2014; Cassidy *et al.* 2014). The 2012 earthquake occurred on a shallow northeast-dipping thrust fault, confirming the presence of some form of convergent strain accumulation offshore of Haida Gwaii. Plate kinematic models place the leading edge of the subducting PA plate east of Haida Gwaii (Fig. 1), assuming subduction initiation between 3.9 and 8 Ma, and a location of convergence initiation between northern Vancouver Island and Haida Gwaii (Smith *et al.* 2003). Despite the geophysical evidence and the occurrence of the 2012 thrust earthquake, the model of oblique subduction beneath Haida Gwaii does not explain all observations in the region. Microseismicity along the west coast of Haida Gwaii occurs predominantly in the vicinity of the QCF (Bérubé *et al.* 1989; Bird *et al.* 1997). In the northern Haida Gwaii region, earthquake focal mechanisms are predominantly strike slip and consistent with the QCF (Ristau *et al.* 2007). In the southern Haida Gwaii region, most earthquakes have thrust mechanisms, though they do not reside on the same fault as that of the 2012 event. There is no clear evidence of Wadati-Benioff seismicity in the region, and all of the observed aftershocks from the 2012 event were observed offshore beneath the Queen Charlotte Terrace, and none beneath Haida Gwaii (Cassidy *et al.* 2014). Furthermore, recent submarine geomorphological mapping suggests plate convergence rates across Haida Gwaii may be significantly less than previously reported, and may be insufficient for subduction initiation (Brothers *et al.* 2020). Understanding the extent (or existence) of subduction has implications for the tectonic history, structure, and dynamics of the region including the size of major seismogenic zones along the margin. Constraining the transition from pure subduction beneath southern Vancouver Island to transpressive deformation near Haida Gwaii is an important objective for understanding the hazards posed by large earthquakes along the west coast of Canada.

3 SURFACE WAVE DISPERSION DATA

Regional earthquakes typically release surface wave energy over period ranges that are sensitive to crustal and uppermost mantle depths,

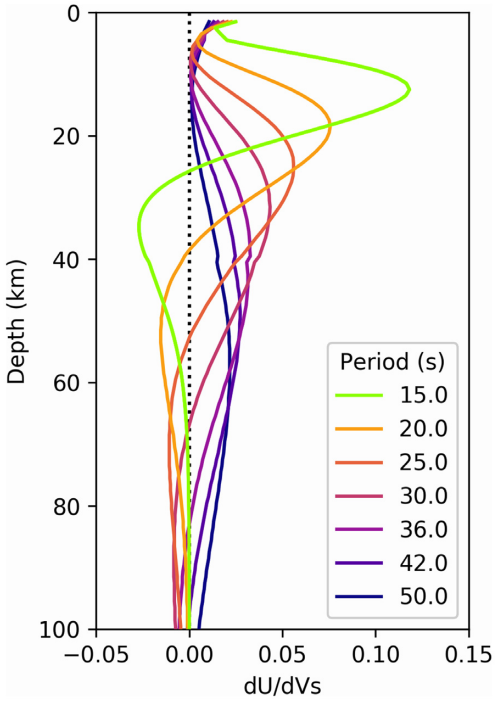

Figure 2. Fundamental-mode Rayleigh wave group-velocity depth sensitivity for periods considered in this work, calculated using a simple 40-km-thick crustal model (available in the supplementary material).

making the dispersion measurements obtained from regional earthquakes useful for studies of tectonic structure (Fig. 2). In general, group velocity dispersion is simpler to measure than phase velocity dispersion, as no information on the earthquake source–time function is required. Since the source group time (the earthquake effect on surface wave traveltime) is effectively negligible for earthquakes shallower than approximately 25 km, for periods less than approximately 75 s (Levshin *et al.* 1999), a wide range of earthquakes can be considered (including those without centroid moment tensor solutions). In contrast, accurate information of the source phase is required for single-station phase velocity measurements from earthquakes. Phase velocity (and group velocity) dispersion measurements can also be obtained via multistation interferometric approaches (e.g. Bensen *et al.* 2007), where source phase information is factored out of the processing procedure. These techniques require concurrently operating seismic stations. Unfortunately, many of the broad-band seismic stations in western Canada considered in this work were temporary deployments that predominantly did not run simultaneously (Fig. 1). Measurement errors for group velocity dispersion are typically larger than for phase velocity measurements (e.g. Bensen *et al.* 2008). The interpretation of group velocity maps is also more complex (due to the negative depth sensitivity even in fundamental mode sensitivity kernels). Nonetheless, group velocity dispersion is a valuable measurement that leads to improved data path coverage in tomographic inversions, which is particularly valuable in this study as station coverage along the west coast of Canada is sparse (Fig. 3).

We used recordings of regional earthquakes from over 300 broadband seismic stations from both permanent and temporary campaign networks with varying deployment times (see supplement for a complete list of stations used in this study). For each station, we used events with magnitude greater than 4.5 between 2000 and 2019 (see supplement for a complete list of events used in this study). For some stations with long deployment times (i.e. several decades), we analysed over 400 events. The majority of the earthquakes considered here are associated with the JdF ridge and QCF (Fig. 1b). We extract 30-min vertical-component seismograms for each event at each available station. Next, we remove the instrument response from each seismogram and apply a zero-phase bandpass filter for periods 5–100 s to suppress microseismic noise and long-period instabilities. Assuming the vertical-component recording of the surface wave coda is dominated by the fundamental-mode Rayleigh wave, basic group velocity dispersion measurements can be obtained from the maximum amplitude of the wave train envelope as a function of time and period. For a known source–station distance, this time-dependence can be easily converted to (group) velocity. In this study, we measure Rayleigh wave group velocity from regional earthquakes using the multiple-filter analysis technique implemented by Herrmann (2013), which allows for manual selection of the velocity-period envelope range for each seismogram (Fig. S1). This is important as each earthquake is unique, and the period range of surface wave energy recorded at each station can vary. Furthermore, significant quality control is required when considering dispersion data from earthquake recordings, which can be accomplished via visual inspection and manual selection. In total, over 30 000 seismograms were analysed, of which over 8000 yielded usable dispersion curves. Although data processing involves manual selection of dispersion curves in group velocity space, the data are considered as traveltime measurements in the tomographic inversions. This is particularly important as surface wave travel paths are updated within the inversion (as discussed in the next section), and the estimated group velocities from the manual selection assumes surface waves travel along minimum distance great circle paths.

A common practice in tomographic studies that consider regional earthquakes is to bin and average measurements from earthquakes that are in close proximity to each other. This technique is used to reduce the number of data that must be considered in linearized tomographic inversions as well as to reduce the effect of path bias, where the data are dominated by paths over a particular region. However, such binning procedures make characterization of data errors more challenging, and can lead to incorrect data weighting if not accounted for. In an effort to remove outliers from the dispersion data set without altering the measurements themselves, we implement a modified binning strategy. We examine the measurements within each source bin (with a radius of 100 km) recorded at each station individually and discard outlier data using a median absolute deviation threshold of 2.5. However, we do not average the data within each source bin but rather retain each individual measurement. Regardless of this procedure, the final data set may still contain outliers if some source bins do not contain a sufficient number of events (<3). Additional treatment of outliers is considered within the inversion methodology (discussed in the next section). We also discard data that have a propagation path length shorter than five wavelengths. The final number of paths considered at each period after this procedure is shown in Fig. 3. We made group velocity dispersion measurements over the period range between 10 and 80 seconds. However, only periods between 15 and 50 s produced adequate path coverage for tomographic inversions with the aim of resolving anisotropy. Specifically, paths over a wide range of directions are required in order to resolve azimuthal anisotropy in tomographic inversions. In this work, azimuthal path coverage is best over the coastal region of British Columbia including Vancouver Island, Haida Gwaii and the continental shelf (Figs S2 and S3).

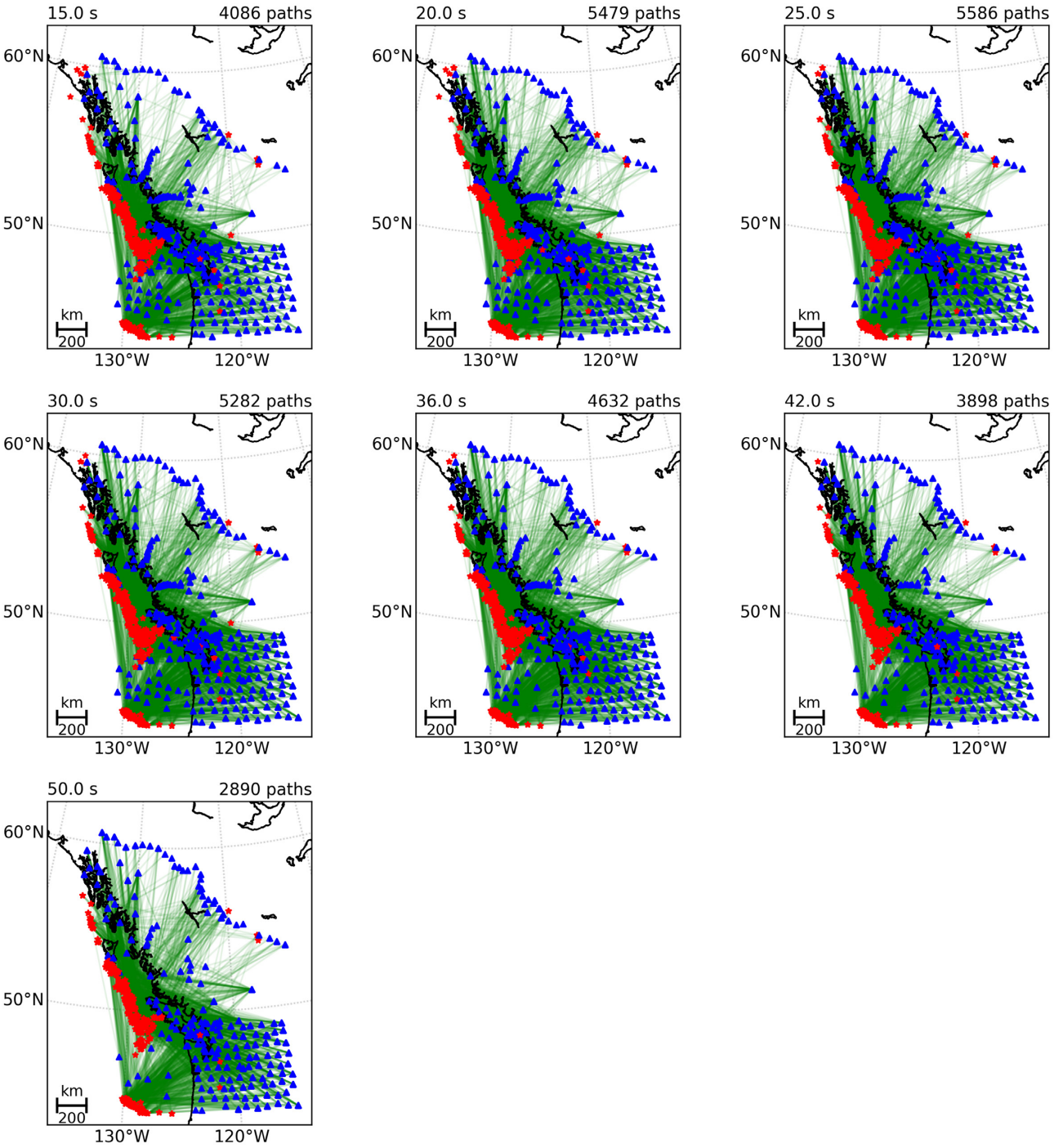

Figure 3. Surface wave path coverage at periods considered in this work. Earthquake locations and recording stations are shown by red stars and blue triangles, respectively. The total number of data considered in the inversion at each period is shown above each map.

4 INVERSION METHODOLOGY

We consider the contributions from isotropic and azimuthally anisotropic components in the inversion of surface wave dispersion data. The parameters that describe the group velocity maps are adaptively defined over a distribution of nodes, where the number and location of the nodes is determined as part of the inversion. Furthermore, we treat the errors in the dispersion data as unknown within the inversion. We solve for all model parameters (including hyperparameters describing the model parametrization and data error distribution) within a Bayesian framework in order to reduce overall model dimensionality (compared to linearized approaches) and avoid subjective regularization procedures. Each one of these steps is detailed in the sections below. Bayesian inversion and associated numerical methods are discussed in Tarantola (2005) and Brooks *et al.* (2011). The specific application of Bayesian inversion to surface wave tomography is discussed in detail in Bodin & Sambridge (2009) and Bodin *et al.* (2012). We note that the inclusion of azimuthal anisotropy within Bayesian

surface wave tomography represents a novel extension of existing methods.

4.1 Azimuthal anisotropy

Seismic anisotropy, in general terms, is the dependence of seismic wave speeds on the direction of propagation. For simplification, studies of seismic anisotropy typically assume hexagonal symmetry and define two types of anisotropy depending on the orientation of the axis of symmetry. Radial anisotropy assumes a vertical axis of symmetry within the Earth, whereas azimuthal anisotropy assumes a horizontal axis of symmetry. Consequently, such definitions of anisotropy can be described by a magnitude and direction. This work considers azimuthal anisotropy, and any reference to seismic anisotropy henceforth is with respect to this type. Under the assumption of hexagonal symmetry with a horizontal axis of symmetry, Smith & Dahlen (1973) approximate the velocity of a surface wave propagating through an anisotropic medium at period T and azimuth ψ to first order by

$$C(T, \psi) = C_0(T) + A_1(T)cos(2\psi) + B_1(T)sin(2\psi) + A_2(T)cos(4\psi) + B_2(T)sin(4\psi), \quad (1)$$

where $C_0(T)$ is the isotropic velocity of the medium. The 2ψ and 4ψ terms represent the velocity variations with π and $\pi/2$ periodicity, respectively. Though eq. (1) was originally defined for surface wave phase velocities, it may be applied to model group velocity in a similar way (e.g. Pawlak *et al.* 2012; Yeck *et al.* 2017; Darbyshire *et al.* 2018). It is recognized that Rayleigh wave data have low sensitivity to anisotropy with $\pi/2$ periodicity, particularly in the mantle where anisotropic signatures are expected to be simpler and lower in magnitude. In the crust, complex interactions of multiple fabrics could produce seismically observable patterns with $\pi/2$ periodicity. However, for computational simplification, we only consider anisotropy with π periodicity and neglect the 4ψ terms in eq. (1). The spatial distributions of three quantities [$C_0(T)$, $A_1(T)$ and $B_1(T)$] are considered in the inversion.

4.2 Model parametrization

In any inversion, a choice must be made in order to define (or parametrize) the model to be solved for. Using a grid with large spacing can result in underfitting the data, where significant resolvable structure is ignored. Conversely, too small of a grid spacing can result in overfitting data, where non-physical signatures in the data (i.e. noise) are fitted, causing spurious model structures. Furthermore, small grid spacing can result in significant additional computational expense. Irregular grids can be applied in tomographic inversions as a geometric approach to impose uniform resolution of model parameters or to estimate model resolution. For example, Debayle & Sambridge (2004) use Voronoi diagrams to qualitatively estimate the length scale of structures that can be resolved in global tomographic inversion by optimizing the Voronoi parametrization to satisfy an appropriate quality criterion. Such a parametrization is defined by a set of nodes with assigned coordinates and values. The model value at any point in space is defined by the assigned value of the nearest node (i.e. nearest-neighbour interpolation), generating a set of discrete geometric cells (Fig. 4). In this case, the size of the individual Voronoi cells is proportional to the resolution length scale for the model parameters. In Bayesian inversion, Bodin & Sambridge (2009) introduced an adaptive model parametrization to seismic tomography also using Voronoi cells. The advantage of this parametrization is that regions in space where the data require additional complexity will be modelled with additional nodes, and vice versa. In this way, the Voronoi cell parametrization is a simple and intuitive means of spatial model adaptation based on data information content.

In practice, however, Voronoi cells possess several undesirable qualities for application to seismic tomography. Foremost, the discrete nature of nearest-neighbour interpolation leads to individual models that appear non-physical. Hawkins *et al.* (2019) recently introduced an alternative means of adaptive model parametrization in geophysical inversion. This approach is similar to Voronoi cells in that it is defined using a distribution of nodes in space. Instead of nearest-neighbour interpolation, a Delaunay triangulation is applied to the nodes and the model quantity [in our case, $C_0(T)$, $A_1(T)$ and $B_1(T)$] at any point in space is linearly interpolated using the velocity values assigned to the nodes of the confining triangle (Fig. 4). The Delaunay triangulation avoids narrow triangles by maximizing the minimum angle of the triangulation. Linear interpolation within the triangles is easily calculated using Barycentric coordinates (Sambridge *et al.* 1995; Hawkins *et al.* 2019). Here we apply the Delaunay triangulation with linear interpolation, which naturally produces more realistic models than Voronoi cells and are preferable in tomographic inversion. Each node is assigned five parameters in total: isotropic group velocity ($C_0(T)$), two parameters describing anisotropy with π periodicity [$A_1(T)$, and $B_1(T)$], and two coordinate values. Similar to Bodin & Sambridge (2009) and Bodin *et al.* (2012) we solve for the number of nodes in the parametrization as part of the inversion, allowing the overall complexity of the model to be determined by the data information content.

4.3 Bayesian inversion

Bayes' theorem can be written as

$$P(\mathbf{m}|\mathbf{d}, H) = \frac{P(\mathbf{m}|H)\, P(\mathbf{d}|\mathbf{m}, H)}{P(\mathbf{d}|H)}, \quad (2)$$

where $\mathbf{d}$ is a random variable (of length N) representing the observed data (in this case, surface wave traveltimes at a particular period of interest) and $\mathbf{m}$ is a random variable (of length M) representing model parameters that describe an anisotropic group-velocity map. Measured data are a fixed realization of $\mathbf{d}$ in practice. Bayes' theorem describes the relationship between conditional and joint probabilities of $\mathbf{d}$ and $\mathbf{m}$, where H is the specific model (e.g. the parametrization or model dimension of the Rayleigh-wave group velocity map). $P(\mathbf{m}|H)$ represents the prior knowledge of the model parameters before the inversion. $P(\mathbf{d}|\mathbf{m}, H)$ represents the likelihood of $\mathbf{m}$, or $\mathcal{L}(\mathbf{m})$ (for model H, since $\mathbf{d}$ is fixed). $P(\mathbf{m}|\mathbf{d}, H)$ is the solution to the inverse problem (the PPD) since it is the probability of the model parameters given a specific model H, prior information, and observed data. $P(\mathbf{d}|H)$ is a normalization term often referred to as Bayesian evidence.

As discussed above, we parametrize the anisotropic Rayleigh-wave group velocity map using Delaunay triangulation with linear interpolation across a set of nodes with associated properties (isotropic velocity, and two anisotropic parameters). The number of nodes in the model is unknown within the inversion procedure, and the level of model complexity is thereby defined by data information content. Consequently, the number of model parameters required to describe the group velocity map is not fixed. Such inversion methods are commonly referred to as trans-d. The number of nodes in the model is a hyperparameter within the inversion that indexes over a countable set of possible model parametrizations (i.e. model H in

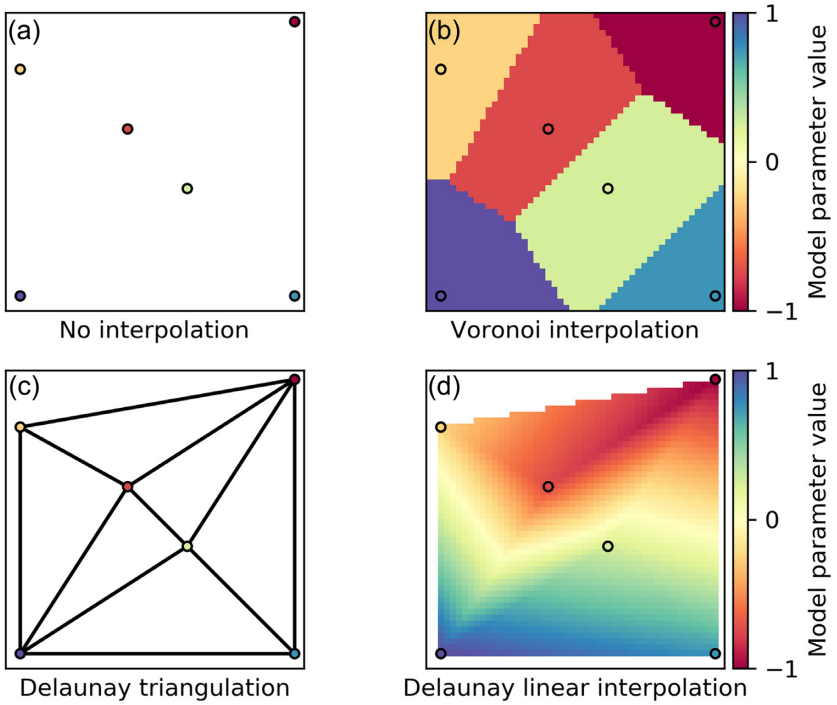

Figure 4. Examples of Voronoi and Delaunay interpolations. A distribution of nodes with randomly assigned parameter values is shown in (a). The corresponding Voronoi interpolation is shown in (b). The corresponding Delaunay triangulation over the nodes is shown in (c). The linear interpolation using Barycentric coordinates within each triangle of the Delaunay triangulation is shown in (d).

eq. 2). In this case, the PPD represents the complete solution to the inverse problem over this set of models and model dimensions. Typically, an analytic solution for eq. (2) does not exist and numerical methods are used to approximate the solution. Specifically, we use the rjMcMC algorithm to draw a series of dependent (on the previous sample) and asymptotically unbiased samples from the PPD (Green 1995, 2003). This algorithm is a generalization of the Metropolis–Hastings sampler, which is a standard McMC technique (Metropolis *et al.* 1953; Hastings 1970). The rjMcMC algorithm involves randomly perturbing a current set of model parameters $\mathbf{m}$ (i.e. the number/position of nodes, and their associated properties) to a new state $\mathbf{m}'$, and accepting this perturbation with probability

$$A(\mathbf{m}'|\mathbf{m}) = \min\left[1, \frac{Q(\mathbf{m}|\mathbf{m}')}{Q(\mathbf{m}'|\mathbf{m})}\frac{P(\mathbf{m}')}{P(\mathbf{m})}\frac{\mathcal{L}(\mathbf{m}')}{\mathcal{L}(\mathbf{m})}|\mathbf{J}|\right], \quad (3)$$

where $Q(\mathbf{m}'|\mathbf{m})$ is the probability of proposing the new state from the current state, and $|\mathbf{J}|$ is the determinant of the Jacobian matrix for the transition between different model states. For model perturbations that do not change the dimension of the model (i.e. moving node positions and changing isotropic or anisotropic parameters), the determinant of the Jacobian is unity. Careful choices of prior and proposal densities also result in the determinant of the Jacobian being unity for perturbations that change model dimensionality (i.e. adding or removing nodes, Bodin & Sambridge 2009; Dosso *et al.* 2014). Specifically, bounded uniform prior distributions are used such that $P(\mathbf{m}) = P(\mathbf{m}')$. Prior bound widths are listed in Table S1, and are selected in order to constrain model parameters to realistic values while still allowing the solution to be predominantly determined by the data. When perturbing a model parameter, a new value is drawn from a Gaussian distribution centered on the current value. In this way, proposal densities are symmetric $[Q(\mathbf{m}'|\mathbf{m}) = Q(\mathbf{m}|\mathbf{m}')]$. In the case of adding a new node to the model, the values of all the parameters associated to this node are drawn from the prior. With the chosen prior and proposal densities, it can be shown that eq. (3) simplifies to a ratio of likelihoods for all types of model perturbations (Bodin & Sambridge 2009; Dosso *et al.* 2014). Given a sufficiently large number of samples, the rjMcMC algorithm provides a good approximation to the PPD.

Within the inversion, the likelihood function depends on the assumed distribution of the data errors, which is typically unknown. The Central Limit Theorem suggests that data errors may follow a multivariate Gaussian distribution, and a likelihood function defined by this distribution is valid. However, in the presence of data outliers, a Gaussian likelihood may be biased. A Laplace distribution is similar to the Gaussian distribution, but with higher probability at greater distance from the mean (i.e. larger tails). Alternatively, the Gaussian distribution can be viewed as the likelihood associated with the L_2 misfit norm, whereas the Laplace distribution is the likelihood associated with the L_1 misfit norm. Consequently, the Laplace distribution is more tolerant of data outliers. As discussed in the previous section, earthquake data from regions with limited seismicity may elude the source binning procedure and introduce outliers into the dispersion data set. For this reason, we apply the Laplace likelihood function in this work, which is given by

$$\mathcal{L}(\mathbf{m}) = \frac{1}{\prod_{i=1}^{N} 2s_i}\exp\left[-\sum_{i=1}^{N}\frac{|r_i|}{s_i}\right], \quad (4)$$

where

$$r_i = d_i^{obs} - d_i(\mathbf{m}) \quad (5)$$

are the data residuals, and s_i is the scale parameter that controls the diversity (i.e. width) of the Laplace distribution for each datum (similar to the standard deviation of a Gaussian distribution). The multiple-filter analysis technique used in this work does not provide useful estimates of the errors on the measured dispersion

data. Furthermore, qualitatively assigning relative errors within the dispersion data set based on uncertainties in earthquake source properties (i.e. location and timing) is not possible as this information is only available for a small number of events in our data set. For these reasons, we implement a parametrized error model within the inversion framework. Similar to Bodin *et al.* (2012), we consider the errors on surface wave traveltimes as unknown and model them using a linear dependence with source-to-station distance Δ_i (for path i) by

$$s_i = a\Delta_i + b. \tag{6}$$

In this way, each traveltime is assigned a different error according to its associated propagation path length. Only two additional hyperparameters (a and b) are considered within the inversion.

4.4 Practical considerations

One of the great challenges with rjMcMC is inefficient sampling over the parameter space, particularly between spaces of different dimensions (in this case, adding or removing model nodes). We attempt to address this issue here by using parallel interacting chains within rjMCMC sampling, often called parallel tempering (Dosso *et al.* 2012; Sambridge 2014). In this method, the acceptance criterion (eq. 3) in each chain is relaxed by raising the likelihood to powers $1/T$ (where T is often called the sampling temperature and is greater than unity). Chains with higher temperatures have greater probability of accepting models that fit the data poorly (low-likelihood), preventing them from becoming trapped in local minima. Probabilistic swapping between the chains allows chains with lower temperatures to efficiently search all regions of the model parameter space. The temperature values for each chain are chosen such that approximately 20 per cent of proposed chain swaps are accepted. This is unique to every problem, and is chosen via trial-and-error. Setting these parameters is subjective. However, in theory, the ultimate choice of these parameters has no effect on the overall inversion solution but only on the efficiency of the algorithm. It is computationally cheap to attempt a swap between chains since data prediction (i.e. forward modelling) is not required. Only chains with temperature set to unity provide unbiased sampling of the PPD. Typically one chain is set at $T = 1$ and only the samples drawn from this chain are kept in the final analysis. Parallel tempering is a robust sampling technique despite the additional computation burden of running multiple chains. For such a large inverse problem with so many model parameters, employing schemes like parallel tempering is valuable for avoiding wasted computation time. This is not only useful for increasing the acceptance rate of adding or removing model nodes to the model, but also allows the sampler to act as a highly effective global optimizer (Sambridge 2014). This greatly reduces the number of initial burn-in samples (dependent on the random initial starting model) required before the algorithm locates the high-likelihood part of the model space.

Previous works that have considered trans-d Bayesian tomography have implemented an iteratively non-linear inversion scheme, where surface wave travel paths are updated after each inversion procedure in order to provide more accurate forward modelling for the following inversion iteration (Bodin & Sambridge 2009; Bodin *et al.* 2012). More recently, Bayesian tomography has been successfully implemented in a fully non-linear inversion where new surface wave travel paths are computed for each new model perturbation in the rjMcMC algorithm, at great computational expense (Galetti *et al.* 2017). Since the data considered in this work are measured from recordings of regional earthquakes (as opposed to ambient noise cross-correlations as in other studies) there are significant uncertainties in the timing and locations of sources that are likely to have a greater effect on the data than the accuracy of the surface wave travel paths (i.e. forward model). Ritzwoller & Levshin (1998) suggest that, other than in extreme cases, off-great circle path propagation can be ignored at periods above approximately 30 s for paths with distances less than approximately 5000 km. Similarly, Bensen *et al.* (2008) suggest that these effects are negligible in surface wave tomography at periods greater than 20 s and path lengths less than 1000 km, which is generally applicable to our group velocity data set over northern Cascadia and Haida Gwaii. It is worth noting that previous studies on trans-d Bayesian surface wave tomography considered much shorter period dispersion data as well as longer propagation paths. However, our study region includes an oceanic–continental transition with potentially large lateral gradients in velocity structure that may produce significant deviations to great-circle ray paths, despite the long periods and short path lengths considered. For this reason (and for the sake of generality of our inversion methodology), we adopt the iteratively non-linear procedure of Bodin & Sambridge (2009) as an optimal balance between accurate forward modelling and computational efficiency. We assume that surface waves travel along great circle paths during the initial iteration. For subsequent inversion iterations, the ray paths are calculated using the inversion solution from the previous iteration. This process is repeated four times to produce the final models.

A consequence of the iteratively non-linear inversion scheme is that data error hyperparameters within the inversion (i.e. a and b values) will be estimated to be larger during initial inversion iterations due to larger theory (forward modelling) errors (Bodin *et al.* 2012). For all inversions in this work, we perform four iterations of ray path updating using a computationally efficient, pseudo ray-bending procedure for piecewise traveltime minimization (Um & Thurber 1987). In order to efficiently perform forward modelling by integrating the traveltime over the surface wave travel paths, we map the Delaunay triangulation with linear interpolation model (discussed above) to a regular, finely sampled, integration grid. We attempted several inversion tests with varying scales of integration grid and found that results do not change significantly once the integration grid spacing is finer than 30 km. At coarser spacing, the linear interpolations within Delaunay triangles become inaccurate. At finer spacing, the forward modelling becomes slower. For all subsequent inversions in this work, we use an integration grid with 30 km spacing. Coincidentally, 30 km is approximately the minimum wavelength of the data considered for northern Cascadia and Haida Gwaii, and represents a physical limitation on the scale of resolvable structure from the data.

The rjMcMC algorithm is used to draw samples from the PPD. Given a sufficient number of samples, a better approximation of the PPD is achieved. It is important to collect enough samples so that the inversion solution becomes stationary (with respect to properties of the PPD). Rigorous quantification of algorithm convergence is an emerging and challenging topic in the field of Bayesian inversion (Brooks *et al.* 2011). It is especially difficult to assess convergence for trans-d inversions, where the PPD spans multiple model dimensions, and a specific parameter in one dimension does not necessarily represent the same structure in a different model dimension (Bodin & Sambridge 2009). We use a similar approach to Bodin & Sambridge (2009) to assess converge of the algorithm by examining

C_0, A_1 and B_1 at given locations in the group velocity map to assess if these quantities are stationary over the rjMcMC samples. Furthermore, we ensure that the distribution over the number of nodes in the model is stationary and provides a smooth distribution. In all inversions discussed here, we ran 20 parallel rjMcMC samplers at varying temperatures to generate 5 million samples each (keeping only those sampled at $T = 1$). The choice of running the inversion with 20 parallel tempering chains stems from the limitations in available computing resources. Inversion tests with fewer parallel chains produce similar results, though they require significantly more samples. Of the retained samples, the first half are discarded as burn-in samples dependent on the (random) initial starting model. Final results for each inversion are represented by the remaining 2.5 million model samples (for the final iteration of updated ray path geometry).

5 SYNTHETIC INVERSION TESTS

Performing tomographic inversions on simulated data (for a known true model) is useful for studying the resolving power of observed data through so-called checkerboard or resolution tests. In this case, synthetic inversions are also valuable for studying and testing new methodologies. In theory, solving for the PPD in Bayesian tomography precludes resolution tests. However, in practice, these tests can help illuminate possible deficiencies in the data, or artifacts in the final model solution. This section demonstrates the Bayesian surface wave tomography with azimuthal anisotropy, and illustrates the spatial resolution for the northern Cascadia and Haida Gwaii data set. The synthetic inversion test presented here is for the source–station path coverage of the data set at a period of 15 s. Tests at other periods show similar results, as the spatial and azimuthal path coverage is similar for the periods considered in this work, even though the total number of data at each period differs (Fig. 3). The true model consists of an alternating checkerboard pattern of slow and fast group velocity anomalies that are ±25 per cent of the average velocity in the 15 s period data set (3.0 km s^{-1}), with a length scale of 360 km. Azimuthal anisotropy in the true model consists of 5 per cent anisotropy (relative to the isotropic velocity) with an alternating opposing pattern of fast-axis directions. The ray paths for the true model are estimated using piecewise traveltime minimization (Um & Thurber 1987), and are used to calculate the simulated data. Gaussian-distributed errors with a standard deviation of 1 s are added to the simulated traveltime data. Furthermore, Gaussian-distributed errors with a standard deviation of 20 s are added to 1 per cent of the data set to simulate outliers. Inversions were carried out using the Bayesian methodology described in the previous section (with four iterations of ray path updating).

Fig. 5 summarizes the results of the synthetic inversion test. The mean values of isotropic and azimuthally anisotropic group velocity extracted from the ensemble of rjMcMC samples at each location in the 2-D map are shown. In general, the inversion test recovers the pattern of isotropic group velocities and azimuthal anisotropy. However, the anisotropic components of the true model are less well recovered, and only resolved in regions with greater azimuthal path coverage. The magnitudes of isotropic anomalies are accurately recovered, especially in regions with dense path coverage. Fig. 5 also shows the estimated model uncertainty for the isotropic group velocity map, and the estimated uncertainty in the orientation of the fast-axis direction of anisotropy. Isotropic group velocity uncertainty is estimated from the standard deviation of the ensemble of rjMcMC samples at each location in the 2-D map. Since the fast-axis direction is a polar quantity estimated from A_1 and B_1 (eq. 1), we propagate the errors in A_1 and B_1 through the simple equation $\frac{1}{2}\arctan(B_1/A_1)$ rather than taking the standard deviation of fast-axis directions themselves. These figures reveal that the estimated model uncertainty depends on the data path coverage as well as the underlying group velocity model. Uncertainty is greater where path coverage is poor. Furthermore, estimated uncertainty is greater near lateral heterogeneity in the velocity model, as the inversion is not able to perfectly recover the location of discontinuous structure.

Fig. 6 shows the distribution of the estimated inversion hyperparameters for the synthetic test. Since the simulated errors on the data were simply Gaussian-distributed, the inversion test correctly estimates no linear relationship between the level of data errors and the length of the data travel paths. The inversion also correctly estimates the constant term for the data errors (b in eq. 6). The slight underestimation of the constant error terms is likely the result of the discrepancy between the simulated error distribution (Gaussian) and the modelled likelihood (Laplace), where the error diversity (modelled by a and b parameters) is smaller than the error standard deviation by a factor of $2^{1/2}$. The results appear insensitive to outliers. However, the effect of outliers within the inversion may be significant if outliers are present in the data in regions with sparse path coverage. Ultimately, the inversion performs well for estimating the unknown level of data errors. Additional synthetic tests were performed using anomalies with a smaller length scale (240 km) under varying noise conditions with Gaussian-distributed errors with a standard deviation of 1, 2 and 5 s added to the simulated traveltime data with outliers as described above (Figs S4 and S5). These tests are shown in the supplement and reveal that the estimation of azimuthal anisotropy in surface wave tomography depends on the tradeoff between the length scale (or magnitude) of anisotropy and the level of data errors. In some cases, the data can be adequately fit without anisotropy when data errors are large (and anisotropy signal is small). Ultimately, the inversion will not recover anisotropy if it is not required by the data, as the mean of the prior distributions for the anisotropic parameters is zero (i.e. no anisotropy). The Bayesian inversion approach allows for detailed examination of the data information content and how this affects the resolution of isotropic group velocity and azimuthal anisotropy.

6 ANISOTROPIC GROUP VELOCITY OVER NORTHERN CASCADIA AND HAIDA GWAII

In this section, we present results for Bayesian tomographic inversion of surface wave dispersion data collected over northern Cascadia and Haida Gwaii. It is challenging to make detailed interpretations from group velocity maps without inverting for a pseudo 3-D velocity model (by estimating 1-D velocity profiles at each location in the study region, then combining them). Interpretation of group velocity maps in our study region is further complicated due to the combination of onshore-offshore structure, where water depth and thick accretionary sediments can have a significant effect on surface wave velocities (e.g. Yeck *et al.* 2017; Darbyshire *et al.* 2018; Janiszewski *et al.* 2019). As such, we provide only a synoptic interpretation of the isotropic and anisotropic group velocity maps and reserve more detailed investigation for future work. For the periods considered here, surface waves on land are sensitive from mid crustal depths to shallow lithospheric mantle depths (Fig. 2).

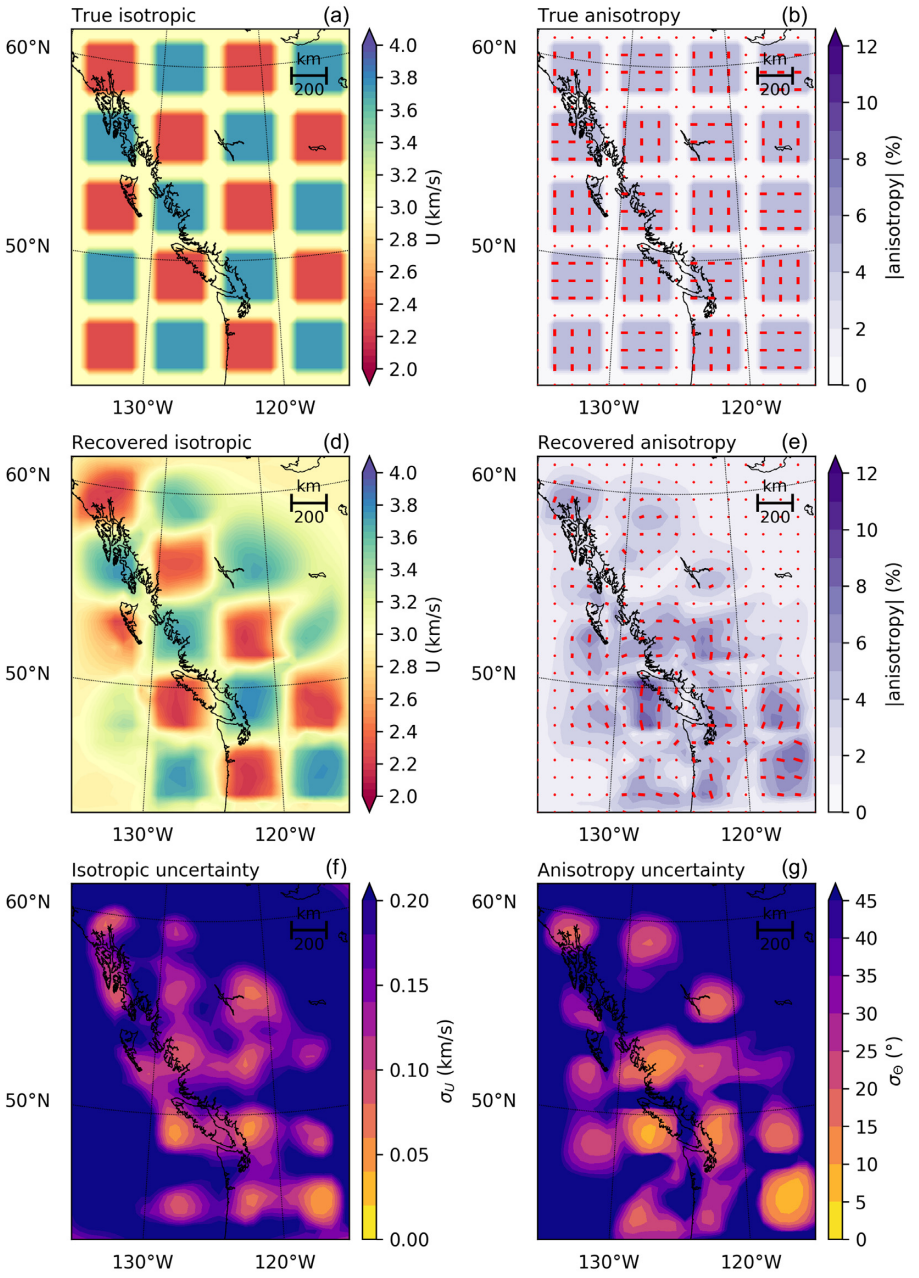

Figure 5. Results of the synthetic Bayesian inversion test. The isotropic and anisotropic components of the true model are shown in (a) and (b), respectively. The surface wave travel paths used to calculate the simulated data set are shown in (c). Mean isotropic velocities estimated from the ensemble of rjMcMC samples for the inversion are shown in (d). Similarly, the recovered fast-axis orientations and magnitudes of anisotropy are shown in (e). The standard deviations of isotropic velocities estimated from the ensemble of rjMcMC samples are shown in (f). The uncertainty of anisotropy fast-axis directions are shown in (g). Red lines delineate the fast direction of anisotropy.

Fig. 7 shows variations in isotropic group velocity as a function of period. At short periods, isotropic group velocity anomalies derive predominantly from compositional variations in the crust, as well as from the presence of sedimentary basins, volcanic provinces, and mountain ranges. At longer periods, surface waves are increasingly sensitive to crustal thickness as well as temperature anomalies in the lower crust and uppermost mantle (Moschetti *et al.* 2007). At periods between 15 and 25 s we observe a significant change in isotropic group velocity along the continental margin that delineates the boundary between oceanic and continental lithosphere (Fig. 7). At 15 s, we observe a narrow band of very slow group velocity, which is likely attributed to water-laden sediments, and sedimentary rocks, along the continental shelf (AC in Fig. 7). This slow velocity anomaly also extends onshore through the Olympic Peninsula south of Vancouver Island, consistent with the location of the onshore Cascadia accretionary complex (Brandon *et al.* 1998). At periods between 25 and 36 s we observe a margin-parallel band of relatively slow group velocity, with higher velocities further inland, throughout the Cascadia margin (CR and FB in Fig. 7). This pattern is consistent with results from other surface wave studies in Cascadia and reflects the presence of the Cascade range (slow) and the Columbia river flood basalts (fast) further inland (e.g. Moschetti *et al.* 2007; Janiszewski *et al.* 2019). At periods between 25 and 42 s we observe a margin-parallel band of high group velocity

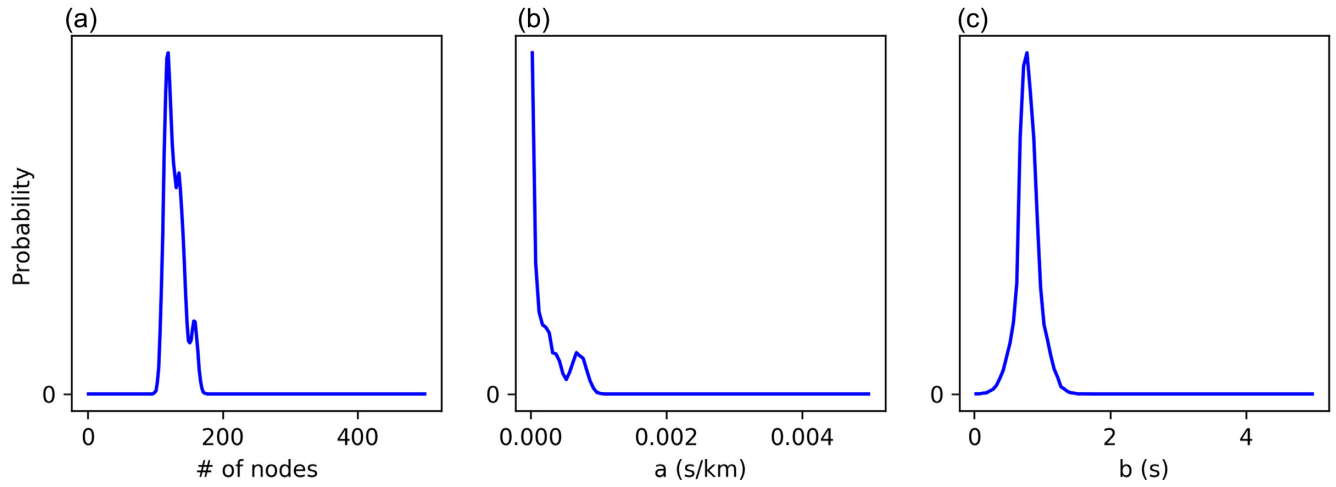

Figure 6. Hyperparameter estimates from the synthetic Bayesian inversion test. The number of nodes in the Delaunay triangulation with linear interpolation is shown in (a). The linear coefficient between unknown data errors and travel path length is shown in (b). The constant term for unknown data error is shown in (c).

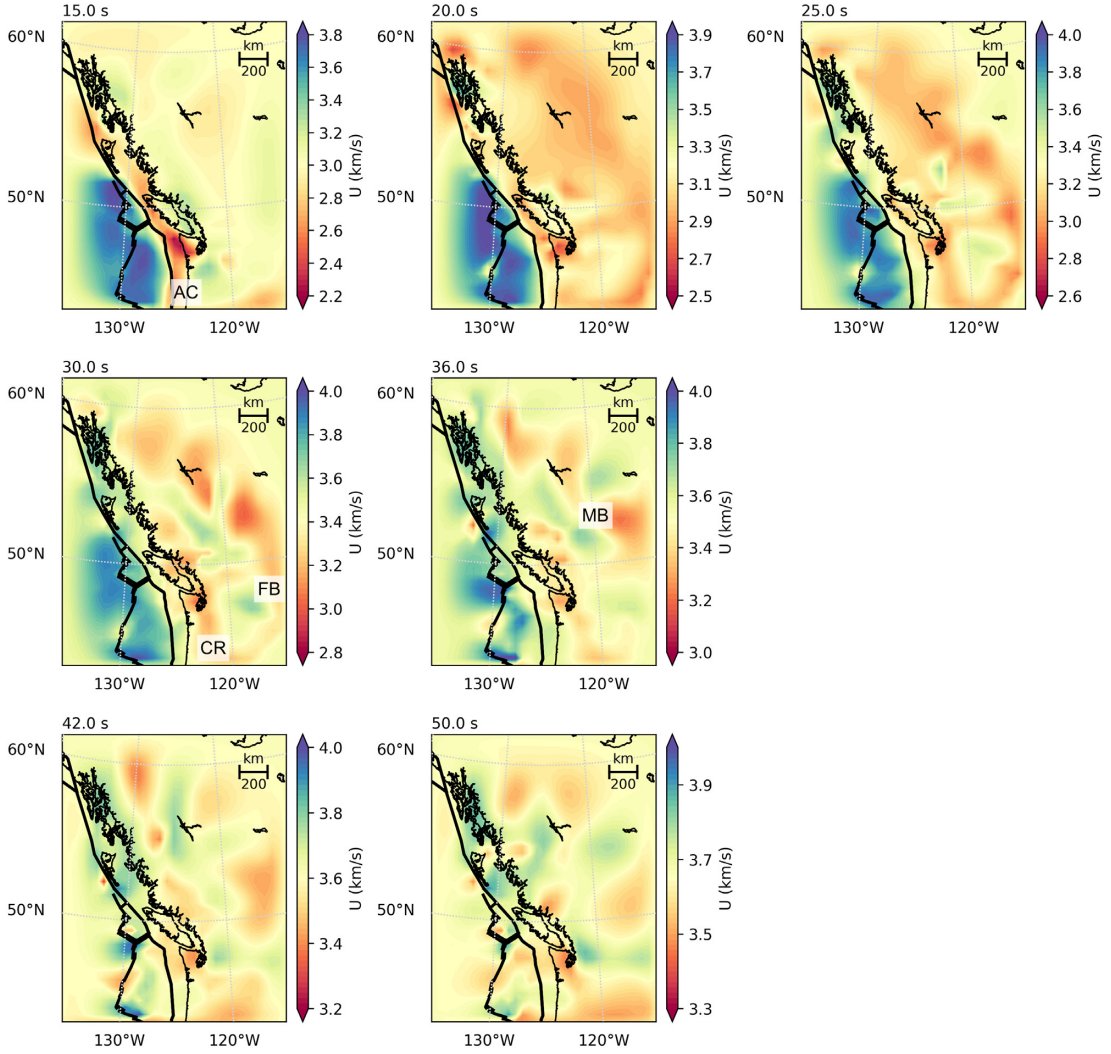

Figure 7. Isotropic group velocity over northern Cascadia and Haida Gwaii. The mean isotropic velocities estimated from the ensemble of rjMcMC samples for inversions at periods 15–50 s are shown. AC, CR, FB and MB stand for accretionary complex, Cascade range, flood basalts and morphological belts, respectively, and are discussed in the text.

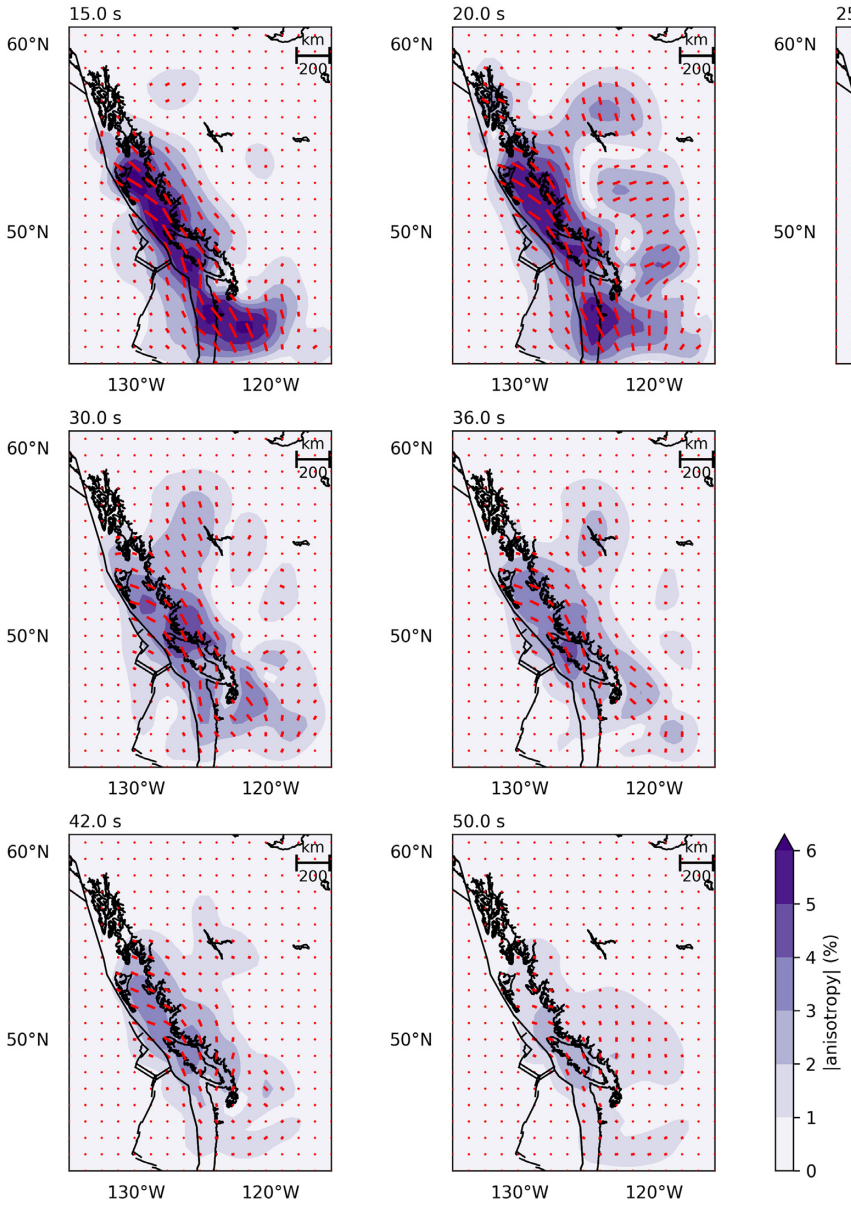

Figure 8. Azimuthal anisotropy in group velocity over northern Cascadia and Haida Gwaii. The mean magnitude and directions of anisotropy estimated from the ensemble of rjMcMC samples for inversions at periods 15–50 s are shown.

over 200 km east of the coast (MB in Fig. 7). The geology of British Columbia comprises a series of margin-parallel morphological belts that contain various accreted terranes (Nelson *et al.* 2013). The observed velocity anomalies likely reflect compositional changes between these belts/terranes or possibly variations in crustal thickness beneath these belts/terranes (Clowes *et al.* 1995). Further detailed examination of the structure of inland British Columbia may be challenging as group velocities are less well resolved here, and may be biased due to the lack of resolvable anisotropy. At the longest periods considered in this work (42 and 50 s), velocity anomalies are generally small in magnitude (note the narrower colour scale range with increasing period) but are generally large in spatial extent, reflecting the large integrated effect of long wavelength surface wave data.

Fig. 8 shows the mean magnitude and directions of anisotropy estimated from the Bayesian inversion. Our anisotropy results show consistent directions across all periods from Vancouver Island to Haida Gwaii, as expected from the overlap in depth sensitivity for the periods considered here (Fig. 2). The slight change in anisotropy direction and magnitude between northern Vancouver Island and Haida Gwaii (most clearly seen at 42 and 50 s in Fig. 8) correlates with a change in isotropic group velocity (42 and 50 s in Fig. 7) and may be a result of the transitional tectonic regime along the coast. At periods considered in this work, seismically observable anisotropy is expected to be attributed to the local compressive stress field, or major foliations within the crust. Local horizontal compressive stress can result in aligned fluid-filled cracks, which produce fast anisotropy directions parallel to the stress direction (Crampin 1994). Throughout northern Cascadia, local shear wave splitting measurements show margin-parallel fast-axis directions (Currie *et al.* 2001; Balfour *et al.* 2012), which are consistent with horizontal compressive stress directions estimated from earthquake moment tensor solutions (Balfour *et al.* 2011). The complicated and low-amplitude pattern of anisotropy recovered over southern

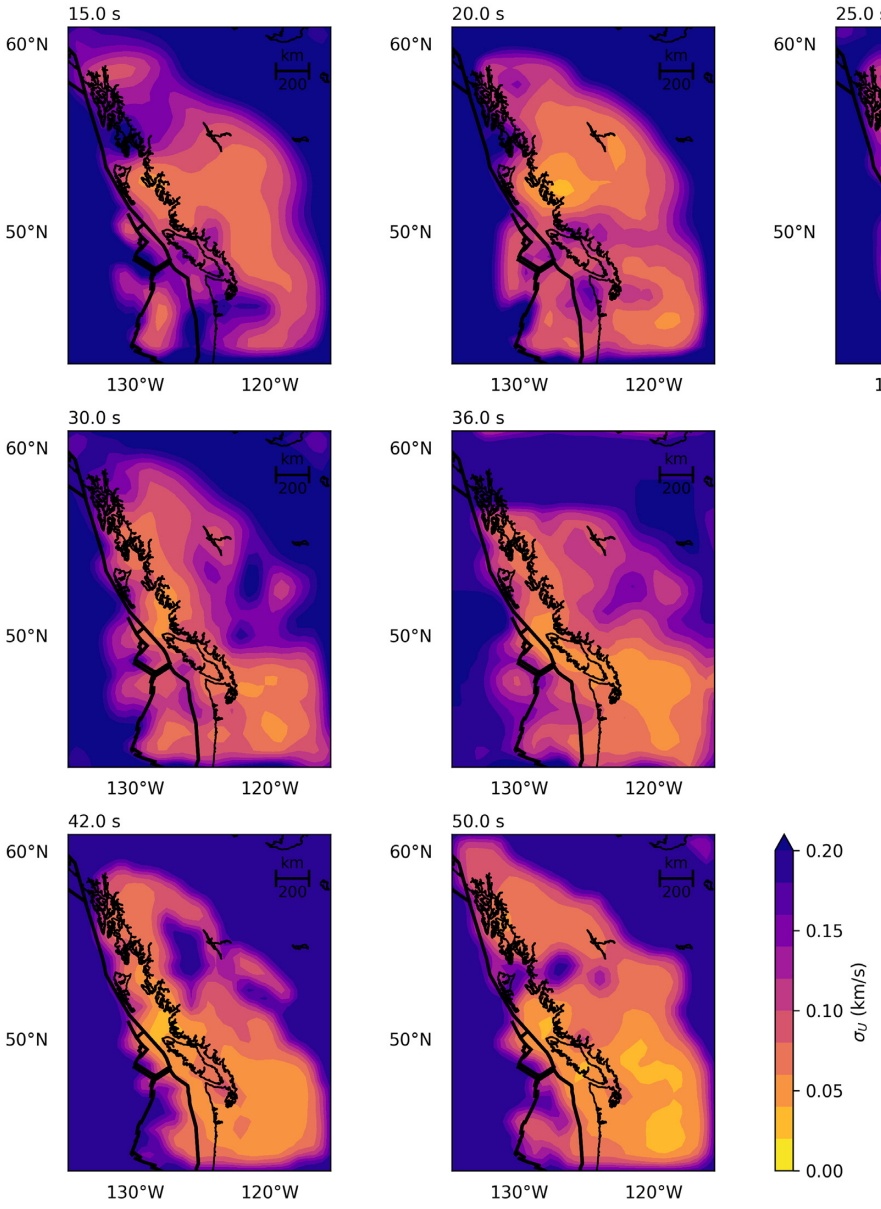

Figure 9. Uncertainty of isotropic group velocity over northern Cascadia and Haida Gwaii. The standard deviations of isotropic velocities estimated from the ensemble of rjMcMC samples for inversions at periods 15–50 s are shown.

Vancouver Island (most notable at 15–25 s) is a robust feature, due to excellent path coverage over this region. It may be the result of superimposed structural anisotropy as some of the stations in this region are located near margin-perpendicular crustal faults with strong anisotropic signatures (Bostock & Christensen 2012). Further north, near Haida Gwaii, limited local shear wave splitting measurements also show margin-parallel fast-axis directions (Cao *et al.* 2017). However, these are perpendicular to local compressive stress directions (Ristau *et al.* 2007), suggesting that crustal anisotropy near Haida Gwaii is the result of structural foliations, possibly related to the QCF. Recent work by Eilon & Forsyth (2020) suggests that shallow offshore anisotropy within and beneath the JdF crust is predominantly margin-perpendicular, though weak in magnitude. Offshore path coverage in our model is not as dense as the continental shelf region, and we suspect such weak offshore anisotropy is likely not resolvable with our data set. In general, our estimates of fast-axis directions in this region appear consistent with local shear wave splitting measurements.

Figs 9 and 10 show the uncertainties in isotropic group velocity and fast-axis direction of azimuthal anisotropy estimated from the standard deviations of the ensemble of rjMcMC samples from the Bayesian inversion. Since the fast-axis direction is a polar quantity estimated from A_1 and B_1 (eq. 1), we propagate the errors in A_1 and B_1 through the simple equation $\frac{1}{2}\arctan(B_1/A_1)$ rather than taking the standard deviation of fast-axis directions themselves. Uncertainty in isotropic group velocity is low throughout Vancouver Island and the continental shelf northward towards Haida Gwaii (Fig. 9). Uncertainties are also low throughout the northwestern United States likely due to the high seismic station density throughout this region (Fig. 3). Uncertainties in the fast-axis direction of azimuthal anisotropy are generally low across all periods for the continental shelf region including Vancouver Island and Haida

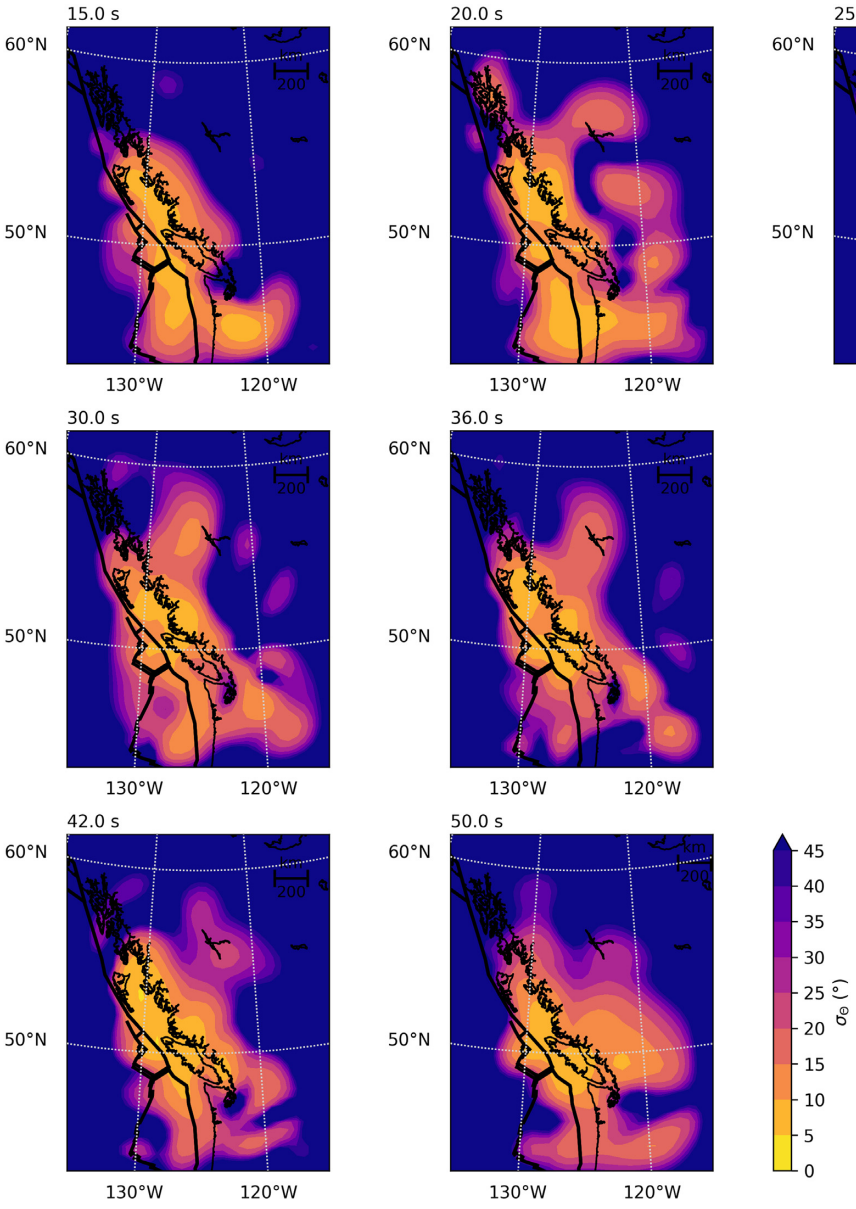

Figure 10. Uncertainty of fast-axis direction of azimuthal anisotropy over northern Cascadia and Haida Gwaii, for inversions at periods 15–50 s.

Gwaii (Fig. 10). However, uncertainties throughout the northwestern United States are higher despite the abundant station coverage. This is likely the result of the lack of azimuthal coverage throughout this region (i.e. all of the ray paths are pointing in a similar direction). This may also be the result of weaker or more complex anisotropy in this region. In summary, only the continental shelf region including Vancouver Island and Haida Gwaii presents low uncertainties in both isotropic group velocity and the direction of azimuthal anisotropy. As such, only results from this region (including associated uncertainties) may be considered for future analysis. Uncertainties in the magnitude of anisotropy are shown in the supplementary material, and are of the order of 1 per cent where recovery is best (Fig. S6). For both the isotropic and anisotropic structure, estimated uncertainties correlate with the recovered isotropic and anisotropic maps, where larger uncertainty is estimated near lateral heterogeneity as the inversion is not able to perfectly recover the location of discontinuous structure.

Fig. 11 shows the distribution of the estimated inversion hyperparameters at each period. In general, all inversions at all periods recover a similar number of nodes in the inversion. The equivalent figure for the distribution of the estimated inversion hyperparameters after 1 inversion iteration (i.e. assuming great circle ray paths) is shown in the supplement (Fig. S7). Comparison between the inversion iterations suggests that, other than for 15 s period data, updating the ray path geometry had little effect on the estimated data errors, as might be expected when considering long period data over short path lengths. It is reasonable then that the inversion of 15 s data should initially recover the smallest number of nodes, since the inversion estimates the largest errors (*a* and *b* parameters) for these data, suggesting that they have reduced information content and are not able to resolve more complex structure. After four iterations of ray path updating, the inversion estimates similar constant terms for data errors, *b* values (Fig. 11c), for all periods. This suggests some consistent, period-independent, source of errors in the data that may

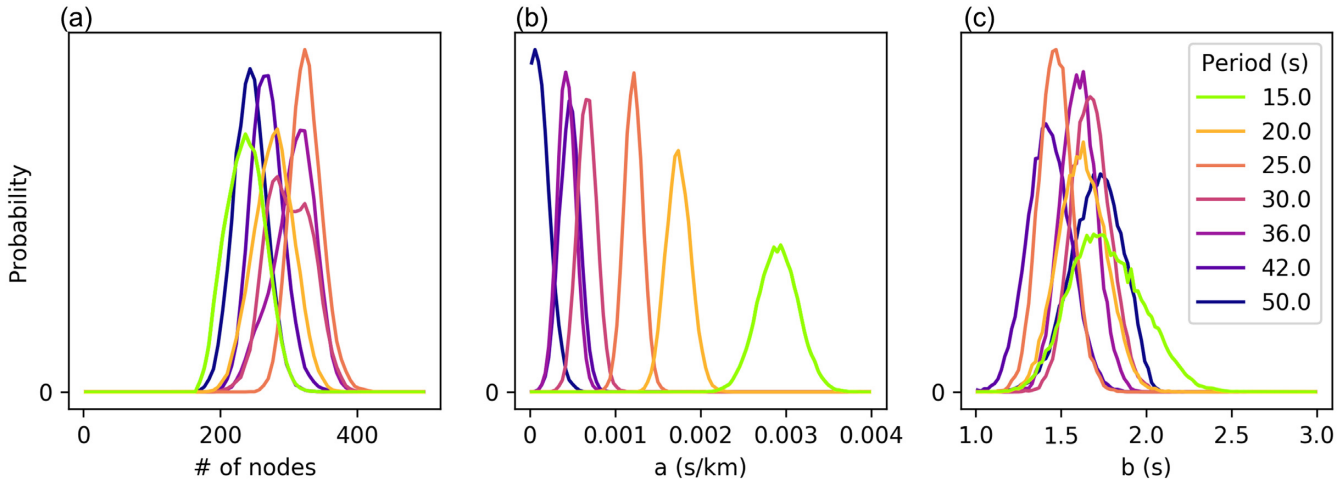

Figure 11. Hyperparameter estimates from Bayesian inversions. The number of nodes in the Delaunay triangulation with linear interpolation is shown in (a). The linear coefficient between unknown data errors and travel path length is shown in (b). The constant term for unknown data error is shown in (c).

be related to errors in source location or onset time. This may be significant as many of the events considered in this work are located offshore and are likely poorly located (and often have analyst-fixed depths). Unfortunately, information on location uncertainty is not available for the majority of the events considered in this work. Fig. 11(b) shows an interesting trend between period and the estimated linear dependence of data errors with travel path length. At long periods, the dependence is estimated to be low (small *a* value), and vice versa. This suggests that surface wave traveltime errors are a function of wavelength, as well as the number of wavelengths between source and receiver. These wavelength-dependent data errors may be attributed to unaccounted-for scattering effects.

7 DISCUSSION AND CONCLUSIONS

In this paper, we consider tomographic inversion of surface wave dispersion data using a novel Bayesian approach to quantify azimuthal anisotropy and associated uncertainty while avoiding subjective regularization procedures. We implement an alternative model parametrization compared to previous work that considered Bayesian tomography in order to produce continuous (more realistic) models. Like previous studies, we consider the inverse problem within a trans-d Bayesian framework, and allowed the model dimensionality (complexity) to be determined by the data information content. Like previous works, non-linearity in the tomographic inverse problem (i.e. ray path geometry) is considered via an iterative process in which paths are updated after each inversion run. It is well known that isotropic structures are better resolved than anisotropic structures using surface wave data. Future work will consider decoupling the parametrizations of isotropic and anisotropic structure. This is similar to Bodin *et al.* (2016) who considered anisotropy in 1-D shear wave velocity profiles constrained by data from single-station seismic methods.

Our inversion method was applied to surface wave dispersion data at periods between 15 and 50 s measured from recordings of earthquakes over northern Cascadia and Haida Gwaii, a region of complex active tectonics but limited station coverage. Group velocity dispersion measurements from regional earthquakes have greater errors than dispersion data obtained from other methods. We consider data errors in a robust way via manual dispersion selection for each seismogram, outlier removal procedures, and the use of a Laplace Likelihood distribution (with unknown diversity estimated within the inversion). Our results for isotropic group velocities are consistent with previous studies further south over Cascadia. Our results for azimuthal anisotropic fast-axis directions are consistent with, and supplement, the limited shear wave splitting measurements over the region. In general, our inversion recovers margin-parallel fast-axis directions between Vancouver Island and Haida Gwaii, with a small change in direction and magnitude along the margin. These results are broadly consistent with azimuthal anisotropy from teleseismic shear wave splitting measurements (Mosher *et al.* 2014; Cao *et al.* 2017), which presumably sample the lithospheric and/or sublithospheric mantle, possibly pointing to vertically coherent deformation.

Our method estimates the unknown level of data errors, and reveals a correlation between surface wave period and the dependence of data errors on travel path length. For periods greater than 15 s, we find that estimated data errors do not change significantly between inversion iterations (i.e. ray path updating) suggesting that for such long period data, over such short propagation path lengths, deviations from the great circle paths are not the dominant source of data errors. The consistency between periods for the estimated constant term of the data errors suggests a systematic source, potentially related to poor event locations (particularly for offshore seismicity). The inversion method provides robust results in regions with sufficient azimuthal path coverage to recover anisotropy. Otherwise, estimated anisotropy is equivalent to the prior distribution (with a mean of zero anisotropy) and recovered isotropic velocities may be biased. Our results demonstrate the value of this novel inversion technique for robust determination of anisotropy from surface wave dispersion data. Our results over the continental shelf, including Vancouver Island and Haida Gwaii, provide an initial step towards resolving a full, 3-D, seismic velocity model in future work. This work provides broad structural context for future seismic station deployments (both onshore and offshore) to study the tectonic structure and dynamics of the region, with the aim of improving our understanding of seismic and tsunami hazards.

Finally, one of the great advantages of Bayesian inversion methods is the ability to incorporate meaningful prior information into the problem. Future work, particularly with respect to structural

studies of northern Cascadia and Haida Gwaii, will consider additional model constraints through the use of informative prior information and other data sets.

ACKNOWLEDGEMENTS

The facilities of the Incorporated Research Institutions for Seismology (IRIS) Data Services, and specifically the IRIS Data Management Center, were used for access to waveform data in this study. IRIS Data Services are funded through the Seismological Facilities for the Advancement of Geoscience (SAGE) Award of the National Science Foundation under Cooperative Service Agreement EAR-1851048. Data from the TA network were made freely available as part of the EarthScope USArray facility, operated by IRIS and supported by the National Science Foundation, under Cooperative Agreements EAR-1261681. Offshore data used in this research were provided by instruments from the Ocean Bottom Seismograph Instrument Center (OBSIC - obsic.who.edu) which is funded by the National Science Foundation. OBSIC data are archived at the IRIS Data Management Center. Seismic waveform data for the Canadian National Seismograph Network are available at the Canadian National Data Centre at: https://earthquakescanada.nrcan.gc.ca/stndon/index-en.php.

This work is supported by the Natural Science and Engineering Research Council of Canada through a Vanier Canada Graduate Scholarship to JMG, and a Discovery Grant to PA.

REFERENCES

Audet, P., 2015. Layered crustal anisotropy around the San Andreas fault near Parkfield, California, *J. geophys. Res.,* **120**(5), 3527–3543.

Audet, P., Bostock, M., Mercier, J.-P. & Cassidy, J., 2008. Morphology of the Explorer–Juan de Fuca slab edge in northern Cascadia: imaging plate capture at a ridge-trench-transform triple junction, *Geology,* **36**(11), 895–898.

Babuska, V. & Cara, M., 1991. *Seismic Anisotropy in the Earth,* Vol. **10,** Springer Science & Business Media.

Balfour, N., Cassidy, J., Dosso, S. & Mazzotti, S., 2011. Mapping crustal stress and strain in southwest British Columbia, *J. geophys. Res.,* **116,** B03314.

Balfour, N., Cassidy, J. & Dosso, S., 2012. Crustal anisotropy in the forearc of the northern Cascadia subduction zone, British Columbia, *Geophys. J. Int.,* **188**(1), 165–176.

Bensen, G., Ritzwoller, M., Barmin, M., Levshin, A.L., Lin, F., Moschetti, M., Shapiro, N. & Yang, Y., 2007. Processing seismic ambient noise data to obtain reliable broad-band surface wave dispersion measurements, *Geophys. J. Int.,* **169**(3), 1239–1260.

Bensen, G., Ritzwoller, M. & Shapiro, N.M., 2008. Broadband ambient noise surface wave tomography across the United States, *J. geophys. Res.,* **113**(B5), doi:10.1029/2007JB005248.

Bérubé, J., Rogers, G.C., Ellis, R.M. & Hasselgren, E.O., 1989. A microseismicity study of the Queen Charlotte Islands region, *Can. J. Earth Sci.,* **26**(12), 2556–2566.

Bird, A., Rogers, G. & Spence, G., 1997. Earthquakes in the Queen Charlotte Islands region: 1984–1996, *Lithoprobe,* **10,** 39–44.

Bodin, T. & Sambridge, M., 2009. Seismic tomography with the reversible jump algorithm, *Geophys. J. Int.,* **178**(3), 1411–1436.

Bodin, T., Sambridge, M., Rawlinson, N. & Arroucau, P., 2012. Transdimensional tomography with unknown data noise, *Geophys. J. Int.,* **189**(3), 1536–1556.

Bodin, T., Leiva, J., Romanowicz, B., Maupin, V. & Yuan, H., 2016. Imaging anisotropic layering with Bayesian inversion of multiple data types, *Geophys. J. Int.,* **206**(1), 605–629.

Bostock, M. & Christensen, N., 2012. Split from slip and schist: crustal anisotropy beneath northern Cascadia from non-volcanic tremor, *J. geophys. Res.,* **117**(B8), doi:10.1029/2011JB009095.

Bostock, M.G., Christensen, N.I. & Peacock, S.M., 2019. Seismicity in Cascadia, *Lithos,* **332,** 55–66.

Bostwick, T.K., 1984, A re-examination of the August 22, 1949 Queen Charlotte earthquake, *PhD thesis*, University of British Columbia.

Brandon, M.T., Roden-Tice, M.K. & Garver, J.I., 1998. Late Cenozoic exhumation of the Cascadia accretionary wedge in the Olympic Mountains, northwest Washington State, *Bull. geol. Soc. Am.,* **110**(8), 985–1009.

Braunmiller, J. & Nábělek, J., 2002. Seismotectonics of the Explorer region, *J. geophys. Res.,* **107**(B10), ETG 1–1-ETG 1-25.

Brooks, S., Gelman, A., Jones, G. & Meng, X.L., 2011. *Handbook of Markov Chain Monte Carlo,* Chapman & Hall/CRC.

Brothers, D.S. *et al.*, 2020. Plate boundary localization, slip-rates and rupture segmentation of the Queen Charlotte Fault based on submarine tectonic geomorphology, *Earth planet. Sci. Lett.,* **530,** 115882,.

Cao, L., Kao, H. & Wang, K., 2017. Contrasting upper-mantle shear wave anisotropy across the transpressive Queen Charlotte margin, *Tectonophysics,* **717,** 311–320.

Cassidy, J.F., Rogers, G.C. & Hyndman, R.D., 2014. An overview of the 28 October 2012 M w 7.7 earthquake in Haida Gwaii, Canada: a tsunamigenic thrust event along a predominantly strike-slip margin, *Pure appl. Geophys.,* **171**(12), 3457–3465.

Clowes, R.M., Zelt, C.A., Amor, J.R. & Ellis, R.M., 1995. Lithospheric structure in the southern Canadian Cordillera from a network of seismic refraction lines, *Can. J. Earth Sci.,* **32**(10), 1485–1513.

Crampin, S., 1994. The fracture criticality of crustal rocks, *Geophys. J. Int.,* **118**(2), 428–438.

Currie, C.A., Cassidy, J.F. & Hyndman, R.D., 2001. A regional study of shear wave splitting above the cascadia subduction zone: margin-parallel crustal stress, *Geophys. Res. Lett.,* **28**(4), 659–662.

Darbyshire, F.A. & Lebedev, S., 2009. Rayleigh wave phase-velocity heterogeneity and multilayered azimuthal anisotropy of the Superior Craton, Ontario, *Geophys. J. Int.,* **176**(1), 215–234.

Darbyshire, F.A., Dahl-Jensen, T., Larsen, T.B., Voss, P.H. & Joyal, G., 2018. Crust and uppermost-mantle structure of Greenland and the Northwest Atlantic from Rayleigh wave group velocity tomography, *Geophys. J. Int.,* **212**(3), 1546–1569.

Debayle, E. & Sambridge, M., 2004. Inversion of massive surface wave data sets: model construction and resolution assessment, *J. geophys. Res.,* **109**(B2), doi:10.1029/2003JB002652.

Dosso, S.E., Holland, C.W. & Sambridge, M., 2012. Parallel tempering for strongly nonlinear geoacoustic inversion, *J. acoust. Soc. Am.,* **132,** 3030–3040.

Dosso, S.E., Dettmer, J., Steininger, G. & Holland, C.W., 2014. Efficient trans-dimensional Bayesian inversion for geoacoustic profile estimation, *Inverse Probl.,* **30,**.

Eilon, Z.C. & Forsyth, D.W., 2020. Depth-dependent azimuthal anisotropy beneath the juan de fuca plate system, *J. geophys. Res.,* **125**(8), doi:10.1029/2020JB019477.

Galetti, E., Curtis, A., Baptie, B., Jenkins, D. & Nicolson, H., 2017. Transdimensional Love-wave tomography of the British Isles and shear-velocity structure of the East Irish Sea Basin from ambient-noise interferometry, *Geophys. J. Int.,* **208**(1), 36–58.

Gosselin, J.M., Cassidy, J.F. & Dosso, S.E., 2015. Shear-wave velocity structure in the vicinity of the 2012 Mw 7.8 Haida Gwaii earthquake from receiver function inversion, *Bull. seism. Soc. Am.,* **105**(2B), 1106–1113.

Green, P.J., 1995. Reversible jump Markov chain Monte Carlo computation and Bayesian model determination, *Biometrika,* **82**(4), 711–732.

Green, P.J., 2003. Trans-dimensional Markov Chain Monte Carlo, in *Highly Structured Stochastic Systems: Oxford Statistical Science Series,* Chapter 6, pp. 179–198, eds Green P.J., Hjort N.L. & Richardson S., OUP.

Hastings, W.K., 1970. Monte Carlo sampling methods using Markov chains and their applications, *Biometrika,* **57,** 97–109.

Hawkins, R., Bodin, T., Sambridge, M., Choblet, G. & Husson, L., 2019. Trans-dimensional surface reconstruction with different classes of parameterization, *Geochem. Geophys. Geosyst.,* **20**(1), 505–529.

Herrmann, R.B., 2013. Computer programs in seismology: an evolving tool for instruction and research, *Seismol. Res. Lett.,* **84**(6), 1081–1088.

Hutchinson, J., Kao, H., Spence, G., Obana, K., Wang, K. & Kodaira, S., 2019. Seismic characteristics of the Nootka fault zone: results from the seafloor earthquake array Japan–Canada Cascadia experiment (SeaJade), *Bull. seism. Soc. Am.,* **109**(6), 2252–2276.

Hyndman, R., 2015. Tectonics and structure of the Queen Charlotte fault zone, Haida Gwaii, and large thrust earthquakes, *Bull. seism. Soc. Am.,* **105**(2B), 1058–1075.

Janiszewski, H.A., Gaherty, J.B., Abers, G.A., Gao, H. & Eilon, Z.C., 2019. Amphibious surface-wave phase-velocity measurements of the Cascadia subduction zone, *Geophys. J. Int.,* **217**(3), 1929–1948.

Karato, S.-I., Jung, H., Katayama, I. & Skemer, P., 2008. Geodynamic significance of seismic anisotropy of the upper mantle: new insights from laboratory studies, *Annu. Rev. Earth Planet. Sci.,* **36,** 59–95.

Kreemer, C., Holt, W.E. & Haines, A.J., 2003. An integrated global model of present-day plate motions and plate boundary deformation, *Geophys. J. Int.,* **154**(1), 8–34.

Leonard, L.J. & Bednarski, J.M., 2014. Field survey following the 28 October 2012 Haida Gwaii tsunami, *Pure appl. Geophys.,* **171**(12), 3467–3482.

Levshin, A.L., Ritzwoller, M.H. & Resovsky, J.S., 1999. Source effects on surface wave group travel times and group velocity maps, *Phys. Earth planet. Inter.,* **115**(3–4), 293–312.

McLellan, M., Schaeffer, A.J. & Audet, P., 2018. Structure and fabric of the crust and uppermost mantle in the northern Canadian Cordillera from Rayleigh-wave tomography, *Tectonophysics,* **724,** 28–41.

Metropolis, N., Rosenbluth, A., Rosenbluth, M. & Teller, A.T.A.E., 1953. Equations of state calculations by fast computing machines, *J. Chem. Phys.,* **21,** 1087–1092.

Montagner, J.-P. & Anderson, D.L., 1989. Petrological constraints on seismic anisotropy, *Phys. Earth planet. Inter.,* **54**(1–2), 82–105.

Montagner, J.-P. & Guillot, L., 2002. Seismic anisotropy and global geodynamics, *Rev. Mineral. Geochem.,* **51**(1), 353–385.

Moschetti, M., Ritzwoller, M. & Shapiro, N., 2007. Surface wave tomography of the western United States from ambient seismic noise: Rayleigh wave group velocity maps, *Geochem. Geophys. Geosyst.,* **8**(8), doi:10.1029/2007GC001655.

Mosegaard, K. & Tarantola, A., 1995. Monte Carlo sampling of solutions to inverse problems, *J. geophys. Res.,* **100,** 12 431–12 447.

Mosher, S.G., Audet, P. & L'Heureux, I., 2014. Seismic evidence for rotating mantle flow around subducting slab edge associated with oceanic microplate capture, *Geophys. Res. Lett.,* **41**(13), 4548–4553.

Nelson, A.R. *et al.*, 1995. Radiocarbon evidence for extensive plate-boundary rupture about 300 years ago at the Cascadia subduction zone, *Nature,* **378**(6555), 371–374.

Nelson, J., Colpron, M., Israel, S., Bissig, T., Rusk, B. & Thompson, J., 2013. The cordillera of British Columbia, Yukon, and Alaska: tectonics and metallogeny, in *Tectonics, Metallogeny, and Discovery: The North American Cordillera and Similar Accretionary Settings*, Vol. 17, pp. 53–109, Society of Economic Geologists Special Publication.

Pawlak, A., Eaton, D.W., Darbyshire, F., Lebedev, S. & Bastow, I.D., 2012. Crustal anisotropy beneath Hudson Bay from ambient noise tomography: evidence for post-orogenic lower-crustal flow? *J. geophys. Res.,* **117**(B8), doi:10.1029/2011JB009066.

Piana Agostinetti, N., Giacomuzzi, G. & Malinverno, A., 2015. Local three-dimensional earthquake tomography by trans-dimensional Monte Carlo sampling, *Geophys. J. Int.,* **201**(3), 1598–1617.

Ristau, J., Rogers, G.C. & Cassidy, J.F., 2007. Stress in western Canada from regional moment tensor analysis, *Can. J. Earth Sci.,* **44**(2), 127–148.

Ritzwoller, M.H. & Levshin, A.L., 1998. Eurasian surface wave tomography: group velocities, *J. geophys. Res.,* **103**(B3), 4839–4878.

Sambridge, M., 2014. A parallel tempering algorithm for probabilistic sampling and multimodal optimization, *Geophys. J. Int.,* **196,** 357–374.

Sambridge, M., Braun, J. & McQueen, H., 1995. Geophysical parametrization and interpolation of irregular data using natural neighbours, *Geophys. J. Int.,* **122**(3), 837–857.

Satake, K., Shimazaki, K., Tsuji, Y. & Ueda, K., 1996. Time and size of a giant earthquake in Cascadia inferred from Japanese tsunami records of January 1700, *Nature,* **379**(6562), 246–249.

Satake, K., Wang, K. & Atwater, B.F., 2003. Fault slip and seismic moment of the 1700 Cascadia earthquake inferred from Japanese tsunami descriptions, *J. geophys. Res.,* **108**(B11),.

Savage, M., 1999. Seismic anisotropy and mantle deformation: what have we learned from shear wave splitting? *Rev. Geophys.,* **37**(1), 65–106.

Savage, M.K., 1998. Lower crustal anisotropy or dipping boundaries? Effects on receiver functions and a case study in New Zealand, *J. geophys. Res.,* **103**(B7), 15 069–15 087.

Savard, G., Bostock, M., Hutchinson, J., Kao, H., Christensen, N. & Peacock, S., 2020. The northern terminus of cascadia subduction, *J. geophys. Res.,* **125**(6), doi:10.1029/2019JB018453.

Schaeffer, A., Lebedev, S. & Becker, T., 2016. Azimuthal seismic anisotropy in the Earth's upper mantle and the thickness of tectonic plates, *Geophys. Suppl. Mon. Not. R. Astron. Soc.,* **207**(2), 901–933.

Smith, A., Hyndman, R., Cassidy, J. & Wang, K., 2003. Structure, seismicity, and thermal regime of the Queen Charlotte transform margin, *J. geophys. Res.,* **108**(B11), 2539.

Smith, M.L. & Dahlen, F., 1973. The azimuthal dependence of Love and Rayleigh wave propagation in a slightly anisotropic medium, *J. geophys. Res.,* **78**(17), 3321–3333.

Tarantola, A., 2005. *Inverse Problem Theory and Methods for Model Parameter Estimation,* Society for Industrial and Applied Mathematics.

Um, J. & Thurber, C., 1987. A fast algorithm for two-point seismic ray tracing, *Bull. seism. Soc. Am.,* **77**(3), 972–986.

Vinnik, L., Makeyeva, L., Milev, A. & Usenko, A.Y., 1992. Global patterns of azimuthal anisotropy and deformations in the continental mantle, *Geophys. J. Int.,* **111**(3), 433–447.

Vinnik, L.P., Farra, V. & Romanowicz, B., 1989. Azimuthal anisotropy in the Earth from observations of SKS at Geoscope and NARS broadband stations, *Bull. seism. Soc. Am.,* **79**(5), 1542–1558.

Yeck, W.L., Sheehan, A.F., Stachnik, J.C. & Lin, F.-C., 2017. Offshore Rayleigh group velocity observations of the South Island, New Zealand, from ambient noise data, *Geophys. J. Int.,* **209**(2), 827–841.

Zulfakriza, Z., Saygin, E., Cummins, P., Widiyantoro, S., Nugraha, A.D., Lühr, B.-G. & Bodin, T., 2014. Upper crustal structure of central Java, Indonesia, from transdimensional seismic ambient noise tomography, *Geophys. J. Int.,* **197**(1), 630–635.

SUPPORTING INFORMATION

Supplementary data are available at *GJI* online.

Figure S1. Example of surface wave dispersion processing from a regional earthquake recording. The location of the earthquake and the recording station are shown by the red star and the blue triangle, respectively. The right-hand panel shows the display of the CPS program (Herrmann 2013). White markers show the manually selected period band for this event at this station. M, AZ, DIST and STA refer to the event magnitude, source-to-station azimuth, distance and station name, respectively.

Figure S2. Surface wave path coverage at periods considered in this work. Hitcounts are shown through the underlying model integration grid (discussed in the text).

Figure S3. Surface wave azimuthal path coverage at periods considered in this work over Vancouver Island and Haida Gwaii. Histograms of source-to-station azimuths through the underlying model integration grid along the transect A–A' are shown. Azimuthal path coverage is best between central Vancouver Island and Haida Gwaii.

Figure S4. Results of synthetic Bayesian inversion tests under varying noise conditions. The isotropic and anisotropic components of the true model are shown in (a) and (b), respectively. Mean isotropic

velocities estimated from the ensemble of rjMcMC samples for inversion tests with Gaussian-distributed noise with 1, 2 and 5 s standard deviations are shown in (c), (e) and (g) respectively. Mean azimuthal anisotropy estimated from the ensemble of rjMcMC samples for inversion tests with Gaussian-distributed noise with 1, 2 and 5 s standard deviations are shown in (d), (f) and (h), respectively. Red lines delineate the fast direction of anisotropy.

Figure S5. Hyperparameter estimates from synthetic Bayesian inversion tests under varying noise conditions. The number of nodes in the Delaunay triangulation with linear interpolation is shown in (a). The linear coefficient between unknown data errors and travel path length is shown in (b). The constant term for unknown data error is shown in (c).

Figure S6. Uncertainty of azimuthal anisotropy magnitude over northern Cascadia and Haida Gwaii. The estimated uncertainty of anisotropy magnitudes estimated from the ensemble of rjMcMC samples for inversions at periods 15–50 s are shown (as per cent anisotropy with respect to isotropic velocity). In general, anisotropy magnitudes are poorly resolved.

Figure S7. Hyperparameter estimates from Bayesian inversions after first inversion iteration (assuming great circle ray paths). The number of nodes in the Delaunay triangulation with linear interpolation is shown in (a). The linear coefficient between unknown data errors and travel path length is shown in (b). The constant term for unknown data error is shown in (c).

Table S1. Prior bounds for model parameters in Bayesian tomographic inversion. C_0 is the isotropic group velocity. A_1 and B_1 are the anisotropic terms for group velocity with azimuthal periodicity of π.

Table S2. Seismograph stations considered for processing of surface wave dispersion from recordings of regional earthquakes. Specific information on each network is available at https://www.fdsn.org/networks/.

Table S3. Regional earthquakes considered for processing of surface wave dispersion.

Table S4. Simple crustal model for surface wave sensitivity kernel estimation (see main text for detail).

Please note: Oxford University Press is not responsible for the content or functionality of any supporting materials supplied by the authors. Any queries (other than missing material) should be directed to the corresponding author for the paper.